Field-amplified sample stacking and focusing in nanofluidic channels

Jess M. Sustarich,[1] Brian D. Storey,[2] and Sumita Pennathur[1,a)]
[1]*Department of Mechanical Engineering, University of California, Santa Barbara, California 93106, USA*
[2]*Franklin W. Olin College of Engineering, Needham, Massachusetts 02492, USA*

(Received 19 May 2010; accepted 6 September 2010; published online 22 November 2010)

Nanofluidic technology is gaining popularity for bioanalytical applications due to advances in both nanofabrication and design. One major obstacle in the widespread adoption of such technology for bioanalytical systems is efficient detection of samples due to the inherently low analyte concentrations present in such systems. This problem is exacerbated by the push for electronic detection, which requires an even higher sensor-local sample concentration than optical detection. This paper explores one of the most common preconcentration techniques, field-amplified sample stacking, in nanofluidic systems in efforts to alleviate this obstacle. Holding the ratio of background electrolyte concentrations constant, the parameters of channel height, strength of electric field, and concentration are varied. Although in micron scale systems, these parameters have little or no effect on the final concentration enhancement achieved, nanofluidic experiments show strong dependencies on each of these parameters. Further, nanofluidic systems demonstrate an increased concentration enhancement over what is predicted and realized in microscale counterparts. Accordingly, a depth-averaged theoretical model is developed that explains these observations and furthermore predicts a novel focusing mechanism that can explain the increased concentration enhancement achieved. Specifically, when the electric double layer is sufficient in size relative to the channel height, negatively charged analyte ions are repelled from negatively charged walls, and thus prefer to inhabit the centerline of the channels. The resulting induced pressure gradients formed due to the high and low electrical conductivity fluids in the channel force the ions to move at a slower velocity in the low-conductivity region, and a faster velocity in the high-conductivity region, leading to focusing. A simple single-channel model is capable of predicting key experimental observations, while a model that incorporates the details of the fluid inlet and outlet ports allows for more detailed comparisons between model and experiment. © *2010 American Institute of Physics*.
[doi:10.1063/1.3496498]

I. INTRODUCTION

The growth in popularity of microfluidics over the past 20 years is due in part to the potential to automate and simplify bioanalytical processes.[1,2] As new micro- and nanofabrication processes are developed, researchers continue to decrease length scales and have achieved functional fluidic devices with features down to several nanometers. As the device dimensions shrink, new physical effects become relevant.[3–5] Due to high surface area to volume ratios, surface charge effects and electric double layers play a prominent role in nanofluidic transport.[5–7] The electric double layer (EDL) is the structure that forms when an electrolyte comes in contact with a charged surface. A diffuse layer of counterions with a thickness characterized by the Debye length forms in the electrolyte in order to screen the wall charge.[8] The Debye length in typical aqueous systems of interest is 10 nm or less. While EDLs are critical in many microfluidic applications, their influence is confined to the boundary when the Debye length is much smaller than the device dimensions. In nanofluidics, the Debye length and device dimension can be on comparable scales and thus the EDL becomes an integral part of the system physics.

The finite size of the electric double layer relative to the channel dimension can cause the transport of ions and charged macromolecules in straight nanofluidic channels to deviate from what is observed at the microscale.[7] These deviations can be exploited for novel bioanalytical devices such as electrophoresis based free-solution DNA separations, protein separations, and confined molecule kinetics.[5,9,10] These devices have simple geometries, yet they remain underutilized and have some aspects which are poorly understood. A better understanding of simple nanofluidic systems can help guide the development and understanding of devices with more complicated geometry.[11–14]

In order to realize many bioanalytical applications with nanofluidics, preconcentration of the analyte may be necessary due to the limited volume and low number of molecules available for detection. The most well known preconcentration technique is field-amplified sample stacking (FASS). FASS was developed in the late 1970s for traditional capillary electrophoresis applications and was optimized by Chien *et al.* in the early 1990s.[15–17] FASS is a relatively simple concentration enhancement method that can be used when the sample has a net charge. The basic principle of FASS is shown in Fig. 1. A straight channel is loaded with a buffer solution containing the sample ions; shown in the middle of the channel in Fig. 1. The buffer solution in the sample re-

a)Author to whom correspondence should be addressed. Electronic mail: sumita@engineering.ucsb.edu.

 © 2010 American Institute of Physics

Downloaded 11 Mar 2011 to 209.94.128.116. Redistribution subject to AIP license or copyright; see http://pof.aip.org/about/rights_and_permissions

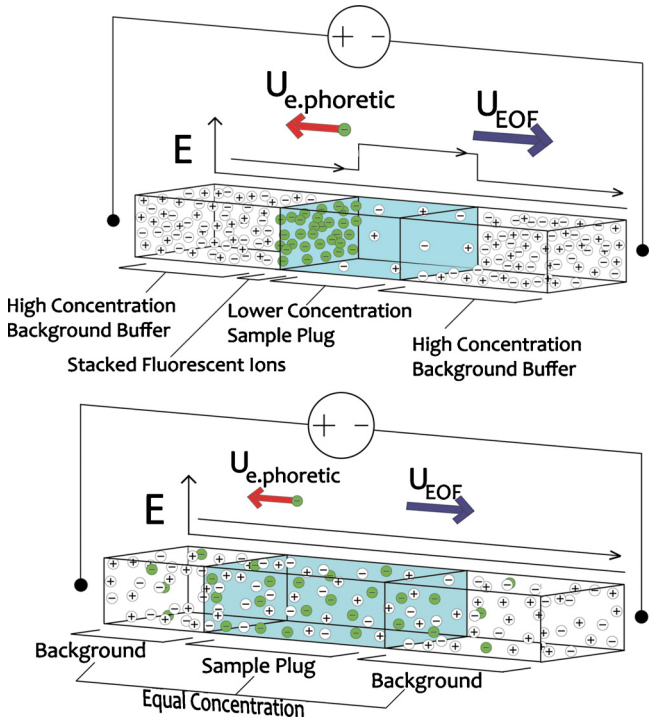

FIG. 1. (Color online) Schematic showing the principle of FASS. (Top) No stacking. In this case, the region containing the charged sample ions is at the same background salt concentration as the rest of the system. In this case, the electric field and the sample ion electrophoretic velocity are the same in both regions. (Bottom) Region containing charged sample ions is at a lower salt concentration relative to the rest of the system, resulting in a nonuniform electric field. The electric field is highest in the low-conductivity sample region since most of the voltage is dropped across the largest resistance. Stacking occurs at the left edge of the low-conductivity region where the sample ions undergo a sudden change in their electrophoretic velocity. The electro-osmotic flow drags everything to the right at constant speed.

gion is set to be at a lower salt concentration than the surrounding background. The charged sample of interest is at a much lower concentration (~ 1 μM) than either buffer (~ 1 mM), and thus the fluid's electrical conductivity is determined only by the local salt concentration. When a voltage is applied across the channel, the electric field has a step-change increase within the low-conductivity region due to higher resistance. This change in electric field is analogous to resistors in series where most of the voltage drop occurs across the largest resistor. The increased electric field results in increased electrophoretic velocity of the sample ions within the low-conductivity region, relative to the high-conductivity background. Thus, the sample ions quickly leave the low-conductivity region and suddenly slow upon reaching the high-conductivity region. This step change in sample ion electrophoretic velocity causes a "traffic jam" and the sample concentration is increased as the ions migrate from the low- to high-conductivity region.[17,18] The term stacking refers to the finite increase in sample ion concentration across the interface between different conductivities.

While the stacking process is occurring, the fluid will be transported down channel via electro-osmotic flow. Since the electric field is highest in the low-conductivity sample region, there is a locally higher electro-osmotic flow in this region. Overall mass conservation, however, demands that the average fluid velocity at any channel location remain constant. Internal pressure gradients are generated in the channel to balance these two effects. These pressure gradients drive a Poiseuille flow that disperses the sample ions and limits the concentration enhancement. The maximum possible sample concentration enhancement in microscale FASS is equal to the ratio of electrical conductivity of the two regions.[17]

There has been much work both experimentally and theoretically to optimize FASS in microfluidic systems.[16,19–27] Burgi and Chien[16] developed a model that determined stacking efficiency in microchannels. Jacobsen *et al.* compared a pinched injection technique to sample stacking in microfluidic systems, finding that sample stacking had superior detection limits.[28] Further studies in the last 10 years have studied the efficiency of sample stacking and the role of dispersion which is caused by internally generated pressure gradients.[18,29] Most recently Santiago and Bharadwaj[18] experimentally validated a model that includes both molecular diffusion and advective dispersion. Other researchers have also considered the electrohydrodynamic stability of flows with electrical conductivity gradients[30–32] that are thought to place limitations on the conditions under which FASS can be realized.[33] However, all work with FASS to date has used a thin electric double layer model, where electrolyte motion can be modeled as flow with a slip velocity condition originating in the EDL.

Sample stacking differs from other concentration enhancement techniques that rely upon focusing. In focusing techniques, the sample ions are driven to an equilibrium point within the system and the concentration enhancement is determined by how strongly the sample is driven to this point versus its tendency to diffuse. Examples of focusing techniques that have been implemented in microfluidic chips include isoelectric focusing[34–36] and temperature gradient focusing.[37] The difference between stacking and focusing is relevant to this work as we demonstrate that nanochannel FASS continuously transitions from a stacking to focusing regime as the channel dimension is reduced. We further note that in FASS, the conductivity gradients are imposed by injecting fluids with different conductivities into the channels. In nanofluidic systems, conductivity gradients can be also be generated within the system by the propagation of concentration polarization[38,39] that can be leveraged for preconcentration applications.[40]

In this paper, we study field-amplified sample stacking in channels with finite sized double layers compared to channel heights. This paper describes new experimental observations and a simple model capable of explaining the key experimental trends. Our approach for experimentally quantifying the spatial and temporal concentration fields involves full field epiflourescence imaging in channels 10–100 times smaller than previously studied.[18,29] We show that nanoscale sample stacking shows critical differences from the microscale in terms of dependence on electrolyte concentration, applied electric field, and channel height. Further, we will demonstrate that FASS at the nanoscale can show marked improvement in terms of concentration enhancement relative

Downloaded 11 Mar 2011 to 209.94.128.116. Redistribution subject to AIP license or copyright; see http://pof.aip.org/about/rights_and_permissions

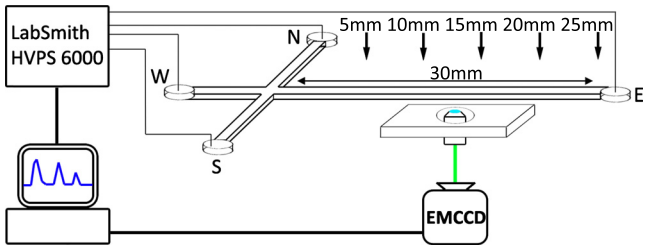

FIG. 2. (Color online) Diagram of the experimental setup. A Prior automated stage (ProScan H117) allowed for real-time observation of the sample as it passed through the detection points of 5, 10, 15, 20, or 25 mm from the intersection. Data were acquired with an Andor Ixon+EMCCD camera mounted on an inverted Olympus IX70 microscope with 60X/1.00 NA water objective. Electrokinetic flow was induced by a HVS448-6000D power supply (Labsmith, Inc.) via platinum electrodes. The channel was imaged through the thinnest (transverse) dimension.

to the microscale due to a novel focusing mechanism that we describe in detail. We explain our observations using a model rooted in the theory of classical electrokinetics. Our model exploits the extreme height to length ratios ($H/L \sim 10\,000$) to achieve a simplified set of equations. The result is a simple model capable of providing useful insight into the physics of the process, which predicts the observed experimental trends, and leads to the identification of key features that can be used to develop nanoscale preconcentration devices.

The paper is organized as follows. In Sec. II, we describe nanoscale and microscale FASS experiments and describe observed differences between the stacking dynamics in micro- and nanoscale conditions. Next, we present the theoretical framework that we used to describe these dynamics. Then we will describe in detail theoretical predictions for both FASS transport in a single channel and FASS transport in the more complicated four-channel system used in experiments, and analyze these results in light of experimental data. We end with a discussion directly comparing our theoretical model to the experimental data, and present areas for future study.

II. MATERIALS AND METHODS

A. Materials

All devices were custom designed in fused-silica wafers using conventional optical photolithography, dry etching, and fusion bonding processing techniques as previously described.[7] A schematic of the channel geometry is shown as part of Fig. 2. Access holes (diameter of 2 mm) were drilled in the 500 μm thick top layer prior to fusion bonding. The volume that resides in the 500 μm deep, 2 mm diameter cylinder serves as the reservoirs for our device. Three different sets of channels were used; dimensions of 20 μm deep by 50 μm wide, 1 μm deep by 9 μm wide, and 250 nm deep by 7 μm wide. For each device the distance between the intersection and the North, South, and West inlets is 5 mm, and 30 mm for the East port, as shown in Fig. 2. The devices were fabricated by a commercial vendor (Dolomite). The tolerances for the depth in the 250 nm channel is ± 50 nm and in the 1 μm channels the tolerance is ± 0.2 μm. The tolerance on the width and length of both channels is ± 0.5 μm. The tolerance in the depth on the shallowest channels introduces the most uncertainty into the problem.

B. Chemicals and reagents

For all experiments, we used potassium phosphate buffer (Sigma Aldrich, Inc.) at pH $\sim$ 7.2 seeded with 5 μM sodium fluorescein salt (Sigma Aldrich, Inc.). Stock solution of 200 mM was prepared using de-ionized filtered water at 18 MΩ/cm provided by a Millipore Milli-Q Gradient filtration system. The stock solution was then diluted to concentrations of 0.5, 1.0, 2.5, 5.0, 10.0, and 25 mM and seeded with 5 μM sodium fluorescein (Sigma Aldrich, Inc.). The pH and conductivity were then measured (Oakton pH and conductivity meter) and the solution was filtered with 0.2 μm polytetrafluoroethylene syringe filter. In our study, sodium fluorescein serves as the sample ion to be experimentally detected.

C. Experimental setup

The experimental setup is diagramed in Fig. 2. The motion and spatial distribution of the sodium fluorescein was imaged using an inverted epiflorescent microscope (Olympus IX70) fitted with a $60\times/1.00$ NA (NA denotes numerical aperture) water objective lens (Olympus, Inc.). Illumination was provided from a 200 W Hg-arc lamp filtered both before and after the sample using interference filters and a dichroic mirror specific to the peak fluorescein absorption and emission wavelengths of 485 and 535 nm, respectively. A ProScan H117 automated stage with a resolution of 0.1 μm was used to monitor the development of the sample ions as they propagate down the East channel. We applied voltages to each well of the nanofluidic channel through platinum electrodes controlled by a multichannel high voltage sequencer (HVS448-6000D, Labsmith, Inc.). A preprogrammed sequence of voltages established the desired fields for flushing, sample loading, gating, and injection/separation estimated using finite element simulations (Comsol, Inc.). Note that since the channels were purchased from a commercial vendor (Dolomite) with specified tolerances, the particular dimensions of the device design allow, for the purposes of this study, consideration of the calculated electric field values to have no error. We acquired intensity data using a back illuminated and intensified EMCCD camera (Ixon+, Andor Co.) with a 512×512 pixel array and 16-bit digitization. Frame rates ranged from 8 to 45 frames per second using a 512×100 pixel subsection of the CCD array. To increase the signal-to-noise ratio, we used on-chip 2×2 binning. Images were corrected using MATLAB by subtracting a background image from the raw data and normalizing by the difference between the flatfield and background image following Ref. 27. To compare the two-dimensional image data with the one-dimensional (1D) model, the intensity data for the pixel regions of the nanochannel images were averaged along the width of the nanochannel to form one-dimensional, area-averaged axial intensity profiles.

Downloaded 11 Mar 2011 to 209.94.128.116. Redistribution subject to AIP license or copyright; see http://pof.aip.org/about/rights_and_permissions

TABLE I. Summary of experimental conditions. Each experiment for the three concentrations listed was performed in both 250 nm and 1 μm channels. For each channel depth/buffer concentration, we used applied electric fields, corresponding nominally to 16 and 32 kV/m (and 48 kV/m for the highest concentration ratio). We imaged the sodium fluorescein at three to five measurement locations. Also shown are electric double layer thicknesses relative to the channel half-height (H) in both the low and high-conductivity regions, as well as the gating times used for each set of experiments.

Channel depth/buffer ratio	Applied E_{Axial} (kV/m)	Detection points (mm)	λ_{hi}/H	λ_{low}/H	t_{Gate} (s)
250 nm/0.5: 5 mM	16	5, 15, 25	0.034	0.106	4.0
	32	5, 15, 25			
250 nm/1: 10 mM	16	5, 10, 15, 20, 25	0.024	0.076	4.0
	32	5, 15, 25			
250 nm/2.5: 25 mM	48	5, 10, 15, 20, 25	0.016	0.050	4.0
1 μm/0.5:5 mM	16	5, 10, 15, 20, 25	0.008	0.026	2.0
	32	5, 10, 15, 20, 25			
1 μm/1:10 mM	16	5, 10, 15, 20, 25	0.006	0.018	2.0
	32	5, 10, 15, 20, 25			
1 μm/2.5:25 mM	48	5, 15, 25	0.004	0.012	4.0

D. Channel and analyte characterization

In order to provide accurate inputs for our model, separate experiments were performed in our laboratory to experimentally determine the surface properties of the channel and mobility of the sample ions. Although these values are listed in the literature,[41] the error bars can be large depending on the exact fabrication method of the channels as well as the manufacturer of the analyte. Therefore, we performed current monitoring experiments[42] and standard fluorescent electrokinetic injection experiments in microchannels to determine the surface charge and zeta potential of the channel, and mobility of fluorescein.[5,43] From these experiments, we find that the flourescein mobility, and estimated flourescein valence are $4.4 \pm 0.06 \times 10^{-8}$ m^2/V s, and $z=-1.75 \pm 0.06$, respectively.[43] Furthermore, we choose a wall charge of between -0.023 and -0.015 C/m^2 corresponding to measured values of -0.02 ± 0.009 C/m^2. Note that although surface charge is known to vary with concentration,[44] our system fits the Grahame equation for the zeta potential with constant surface charge within experimental uncertainty across the range of concentrations used in this work. While the exact values of the surface charge and fluorescein mobility can have an impact on the quantitative comparison between experiments and theory, the general trends and behaviors predicted by the theory are relatively insensitive to these parameters.

E. Experimental conditions

We performed parallel experiments in the 1 μm and 250 nm channels, varying the buffer concentrations and applied voltages for each experiment, as summarized in Table I. While the buffer concentration ratio is always fixed at 10 to 1, three buffer concentration were used; 5 and 0.5 mM, 10 and 1 mM, and 25 and 2.5 mM to create different electric double layer thickness to height ratios, where the Debye length, λ_D, is defined for a symmetric electrolyte as

$$\lambda_D = \sqrt{\epsilon kT/2e^2 z^2 n_\infty}, \tag{1}$$

where ϵ is the permittivity, k is the Boltzmann's constant, T is the temperature, e is the elementary charge, z is the valence, and n_∞ is the number density of ions in the bulk. The concentrations, corresponding double layer thickness relative to the channel half height (H), and other experimental parameters are shown in Table I. Despite the fact that the EDL is always less than 10% of the channel height, the impact will be shown to be quite significant.

The three voltage schemes we apply result in electric fields of approximately 16, 32, and 48 kV/m in the 30 mm long injection channel. These electric fields were estimated using a COMSOL finite element simulation of the entire channel at the time of injection. The dynamics of the electric field are complicated by the fact that the channel contents (and thus the electrical resistance) changes throughout the process. The electric field reported here should only be considered a nominal value and the precise dynamics will be considered later in the paper. The fluorescent sample is observed at three to five locations (5, 10, 15, 20, or 25 mm) from the injection point using the automated stage.

F. Channel preparation and experimental procedure

To prepare the channel for a FASS experiment, we first electrokinetically flush the channels with de-ionized water for 15 min using the loading voltages (see Table II). These voltages were chosen so that all fluid from the North, West, and East ports would flow into the South waste well. Next, we flushed the channel with a solution of 100 mM KOH for 15 min using the same voltage scheme as the loading voltages, but at lower values to reduce the possibility of electrolytic reactions and Joule heating caused by the increased ionic concentration of the unbuffered KOH. The channels were flushed with de-ionized water for an additional 15 min, and current was monitored to ensure that all the KOH exited

Downloaded 11 Mar 2011 to 209.94.128.116. Redistribution subject to AIP license or copyright; see http://pof.aip.org/about/rights_and_permissions

TABLE II. Voltages applied at each well for the various steps described in the experimental procedure. These steps include: (1) loading conditions using during electrokinetic flushing of water and buffer, (2) loading voltages reduced by a factor of 3 for flushing with 100 mM KOH, (3) gating voltages used to inject sample into the East channel with the gating time provided in Table I, and (4) injection voltages used to drive the low-conductivity plug and sample down the East well. The different injection voltages resulted in different electric fields within the East channel during injection, nominally, 16 kV/m, 32 kV/m, and 48 kV/m, respectively.

	Inlet voltages (V)			
Flow scheme	V_{North}	V_{East}	V_{South}	V_{West}
Loading	828	1500	0	752
KOH Flush	276	500	0	251
Gating	1000	−3000	300	1000
Injection 16 kV/m	280	0	280	1000
Injection 32 kV/m	560	0	560	2000
Injection 48 kV/m	840	0	840	3000

the channel. Next, the reservoirs were thoroughly rinsed with de-ionized water to ensure that no trace amounts of KOH were present. To rinse the reservoirs, we pipetted approximately 20 μL of solution into and out of the well four to five times. Next, the interface between high- and low-conductivity buffer regions was generated with potassium phosphate buffer solution, driving the lower conductivity buffer containing the sample from the North to the South well, and the higher conductivity buffer from the West and the East to the South well (Fig. 3, step a). After this step, each port was rinsed with its respective buffer by pipetting the appropriate solution into and out of the well a few times, and flushing the channel (using loading voltages) for 5 min. This cycle was repeated three times before experiments were performed to ensure the desired concentration in each channel. The desired state was confirmed through fluorescence intensity measurements as well as by observing a steady state current (Keithley 2410, Keithley, Inc.). Once a conductivity interface was established, a gating method was necessary to inject enough low-conductivity buffers into the channel to allow for fluorescein to enter the East channel [Fig. 3(b)]. Once enough fluorescein entered the East channel, injection voltages were used to propagate the plug down the channel [Fig. 3(c)].

Prior to data collection, the focus at the channel intersection was matched to that of the channel 25 mm downstream to ensure that intensity data would be in the same depth of focus for each experiment. This leveling was done via set screws in the devices' mounting chassis. Each experiment shown in Table I was performed three times to ensure repeatability. Table II provides the voltages used in our experiments for each step.

Gating is required in nanochannels to allow enough low-conductivity solution to enter the East channel. Images of the fluorescein distribution during the gating process in a 250 nm and 1 μm channel are shown in Fig. 4. Different gating times were needed for different experiments to ensure that enough sample enters the channel for analysis. When the gating voltages are turned on, the electrophoretic velocity of

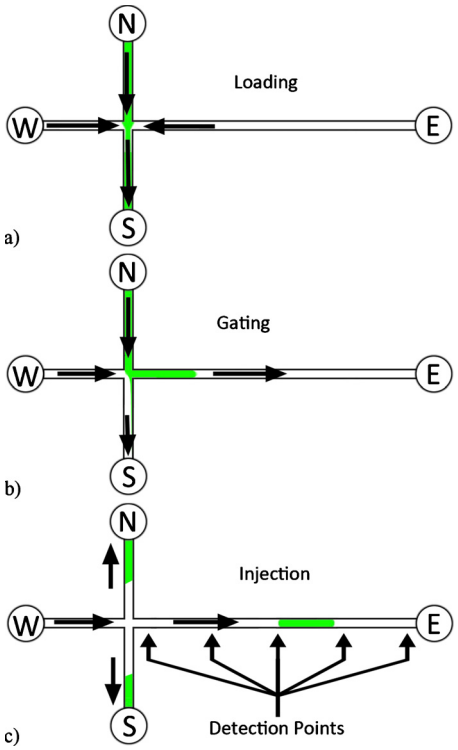

FIG. 3. (Color online) Schematic of sample injection sequence with flow direction denoted with arrows and the low-conductivity sample region is denoted by the shaded area. (a) First, the low-conductivity sample is loaded from the North well to the South well. In this step, high-conductivity buffer is flowing from both the East and West wells toward the South well. (b) Next, gating is performed for several seconds in order to inject a long plug of low-conductivity containing the fluorescent sample. Low-conductivity fluid and sample ions enter the East channel from the North well. (c) Finally, the sample is injected by switching to the injection voltages. Here, high-conductivity buffer flows from the West to the East channel, closing off the introduction of sample from the North well and allowing for the sample to propagate as a plug down the channel. Actual voltages applied for each of these steps (loading, gating, injecting) are shown in Table II.

the fluorescein is greater than the electro-osmotic velocity of the fluid in the East channel. Since the fluorescein and the walls are negatively charged, the sample ion electrophoretic velocity is always opposite the electro-osmotic velocity. At the initial gating time, fluorescein cannot enter the East channel because the electrophoretic velocity exceeds the electro-osmotic flow. The fluorescein is focused in the center of the channel (as seen in the first few frames of Fig. 4) and it flows toward the South. As the East channel fills with low-conductivity buffer the electric field and the flow change along with the electrical resistance. Eventually, a condition is reached where the electro-osmotic flow velocity in the East channel is greater than the electrophoretic velocity of the sample, and the sample ions are dragged into the East channel by the fluid. We capture this effect in our model, as we will discuss more fully in Sec. VI B.

One important observation is that while gating time is carefully controlled, the movement of sample ions from the South channel to the East exit channel is not consistent between experiments (see Fig. 4). The exact amount of sample injected into the channel, as well as the amount of low-conductivity fluid is an experimentally unknown parameter

Downloaded 11 Mar 2011 to 209.94.128.116. Redistribution subject to AIP license or copyright; see http://pof.aip.org/about/rights_and_permissions

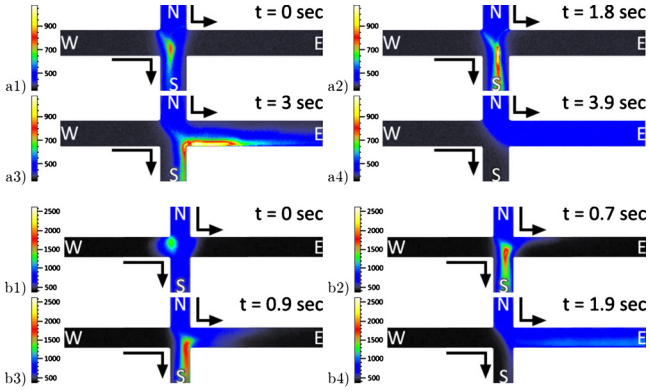

FIG. 4. (Color online) Experimental images of gating in 250 nm and 1 μm channels using a 1 to 10 mM buffer concentration ratio in all cases. a) Experiments in a 250 nm channel, showing the details of the gating step [Fig. 3(b)]. (a1) In the first frame (t=0), the voltages are switched from loading to gating (See Table II), and there is an immediate focusing of fluorescein in the center of the channel. Although the low-conductivity buffer is flowing from the North well to the East well [Fig. 3(b)], the fluorescein is not entering the channel. (a2) In the second frame (t=1.8 s), we observe more fluorescein focusing in the center of the channel, but none in the East channel. (a3) Only in the third frame, at t=3.0 s, do we see the fluorescein begin to flow into the East channel. (a4) As the East channel continues to fill with low-concentration buffer, more fluorescein flows in the channel (t=3.9 s), just before the plug is injected (high-conductivity buffer from the west well closes the North channel, creating a plug of sample.) (b) Same experiment in a 1 μm deep channel. Here, we observe behavior similar to that of the 250 nm deep channel, although the fluorescein enters the channel at a much earlier time (t=1.9 s).

in our study, although it could possibly be better controlled in future work. In our case, this unknown leads to complications with comparisons to the theoretical modeling, described in Sec. VI B. Although this gating operation creates an interface that is not completely discrete, we assume that these effects are negligible compared to the axial length scales in our modeling.

III. EXPERIMENTAL RESULTS

Figure 5 shows raw data collected from an experiment in a 250 nm deep channel (left column) and 1 μm deep channel (right column) for a 1–10 mM concentration ratio at two different applied electric fields. The y-axis is normalized to the initial fluorescein intensity, and thus represents the amount of concentration enhancement. The different peaks correspond to observations of the same sample plug (during a single experiment) at different points in the channel. Although Fig. 5 shows only one realization of an experiment, three experiments were performed at each condition (all experimental realizations with error bars can be seen in Fig. 7). From Fig. 5, we note the following observations, which are consistent with experiments performed at the two other buffer conditions. First, the overall concentration enhancement is significantly larger in the nanochannel versus the microchannel. Second, in the nanochannel the maximum concentration is always located further downstream of the injection point than in the case of the microchannel. Third, increasing the electric field strength increases the amount of concentration enhancement and the position of the maximum intensity peak in the nanochannel, whereas it has little or no effect in the microchannel. What is most interesting is that the concentration enhancement of the nanochannel exceeds the theoretical maximum of classical microchannel FASS (given by the conductivity ratio, which is 10 in our case). Note that the shape of the intensity in the nanochannel 5 mm from the injection point has a sharp, high intensity peak followed by a long low intensity region, corresponding to the gated injection that was required. In the microchannel, this shape is not apparent due to the plug reaching its peak concentration enhancement before 5 mm. This difference is likely due to the difference in gating time and will be discussed more fully later.

As the double layer to channel height ratio increases (i.e., lower buffer concentration at a given channel height), the maximum intensity increases. This trend can be observed in Fig. 6, which shows the concentration enhancement in a micro and nanochannel for all of our experimental conditions. Figure 6(a) shows the concentration enhancement at a fixed location 15 mm downstream of the injection point, and Fig. 6(b) shows the overall maximum enhancement at any location. The nanochannel has a greater concentration enhancement in all cases, but most notably for low concentrations and high electric field strengths. We also see that the concentration increase does not change much over the entire set of experiments for a microchannel, but it does for a nanochannel, confirming our observations that the electric field, channel height, and buffer concentration affects nanochannel FASS but not microchannel FASS. The classic picture of microchannel FASS is that the maximum possible concentration enhancement is given by the conductivity ratio of the two buffer solutions (which is 10 in our experiments) but dispersion limits the realization of this maximum.[17] Our data in the 1 μm channel is consistent with the classic model.

For completeness, Fig. 7 shows the maximum concentration that was achieved in 250 nm and 1 μm deep channels over all of our experiments at all channel locations. It is important to notice the different scales of the y-axis, with the highest normalized intensity in the microchannel case being less than 10, whereas it is approximately 200 for the nanochannel case (plotted in inset). We also observed that the improved performance of the nanochannel begins to breakdown when the overall concentration is increased. Using a 2.5 mM buffer concentration in the sample region and a 25 mM buffer concentration in the background region, the sample enhancement between micro- and nanochannel is only about 1.5 using a high electric field (48 kV/m). Note that a higher applied field was necessary in this case, due to the decrease of electro-osmotic mobility at higher buffer concentrations.

From Figs. 6 and 7, we notice that the high electric field leads to greater concentration enhancement for all cases, but in the nanochannels, there is a greater effect. Furthermore, as observed in Fig. 5, the location of maximum concentration is generally located further downstream in a nanochannel versus microchannel. In microchannels, the concentration enhancement occurs right away, and then diffusion takes over and reduces the maximum concentration.[18] However, in a nanochannel, the concentration enhancement does not necessarily occur at the injection point. It is sensitive to concen-

Downloaded 11 Mar 2011 to 209.94.128.116. Redistribution subject to AIP license or copyright; see http://pof.aip.org/about/rights_and_permissions

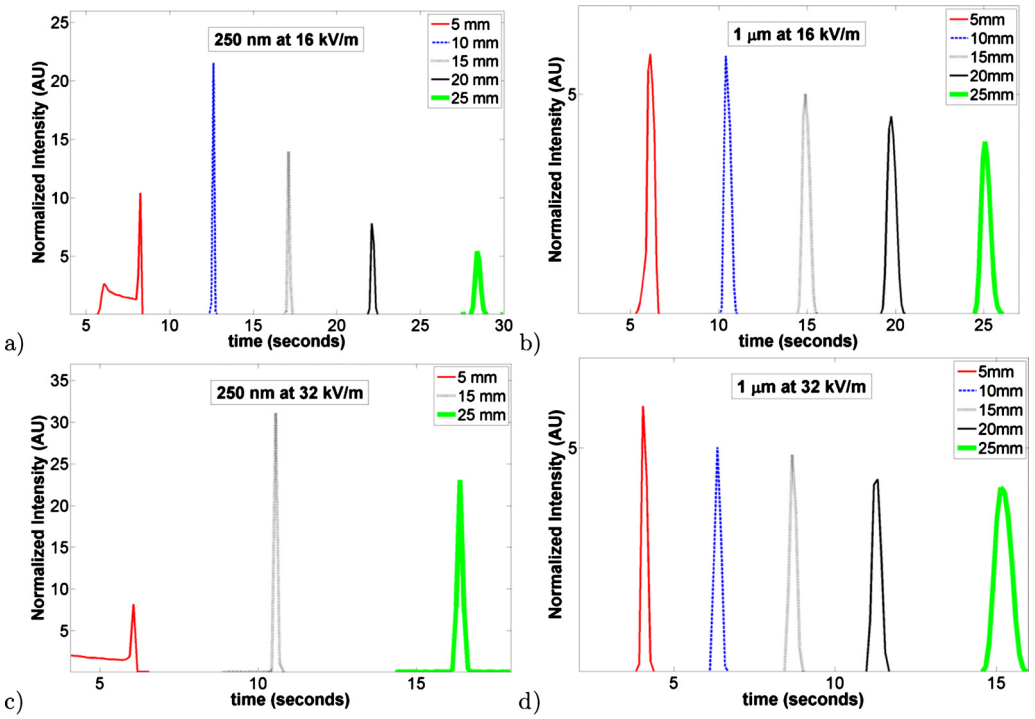

FIG. 5. (Color online) Intensity vs time for different channel depths and electric fields. All four cases use a 1 to 10 mM concentration ratio. All data show evolution of the same injected fluorescent plug over time at 3–5 locations. (a) 250 nm deep channel with 16 kV/m applied electric field. (b) 1 μm deep channel with a 16 kV/m applied electric field. (c) 250 nm deep channel with 32 kV/m applied electric field. (d) 1 μm deep channel with a 32 kV/m applied electric field. Note that increasing the electric field in the microchannel does not change the behavior, while in the nanochannel a higher electric field gives a higher intensity. At both electric fields the enhancement is much higher in the nanochannel. Similar observations were noted for other concentrations.

trations used, the electric field, and the channel height, not just the conductivity ratio. In all cases, nanochannels have better performance than microchannels. The remainder of the paper will be devoted to explaining these observations.

A. Instability observations

It should be noted that parallel experiments in 20 μm deep channels with the same gating voltages were not successful due to apparent mixing of the low- and high-conductivity buffers during the gating sequence. When voltages 1/8th of the gating voltages listed in Table II were applied, instabilities were still observed. These observations are likely electrohydrodynamic instabilities that occur in flows with conductivity gradients and applied electric fields.[30–33] These instabilities have been implicated as a reason for breakdown of classic FASS as the conductivity gradient is increased.

This mixing behavior was not observed in the 1 μm or 250 nm channels. However, it is possible that some mixing occurred in our channels but could not be detected due to the lower signal to noise ratio. Previous work on electrohydrodynamic instabilities has shown that the instability depends primarily on the critical electric Rayleigh number. This parameter scales as H^2 (where H is channel height).[30–33] It thus seems reasonable that the smaller channels are significantly more stable. Less apparent instability in the smaller channels is another advantage for their use in FASS and may allow for the use of higher conductivity ratios. Pushing nanochannel FASS to higher conductivity ratios and exploring instability is an area for future work.

IV. THEORETICAL FRAMEWORK

The description of experimental data serves as an introduction to the problem and describes observed features of nanoscale FASS. We now turn to a theoretical framework to describe our observations, starting with the general governing equations for the evolution of ionic species in FASS. Since our experimental channels are much longer ($\sim$10 mm) than they are deep ($\sim$100 nm), we use the thin channel approximations to obtain a set of simplified equations that is suitable to describe salt transport, sample transport, and bulk flow.

A. Governing equations

The basic governing equation for the rate of change of the number density of the charged species is the Nernst–Planck equation,

$$\frac{\partial n_i}{\partial t} + \mathbf{u} \cdot \nabla n_i = D_i \nabla \cdot \left(\nabla n_i + \frac{z_i e}{kT} n_i \nabla \Phi \right). \tag{2}$$

Here, n is the number density, $\mathbf{u}$ is the velocity vector, D is the diffusivity, k is the Boltzmann's constant, T is the temperature, e is the elementary charge, z is the valence, Φ is the electric potential, and the subscript i denotes the species. The

Downloaded 11 Mar 2011 to 209.94.128.116. Redistribution subject to AIP license or copyright; see http://pof.aip.org/about/rights_and_permissions

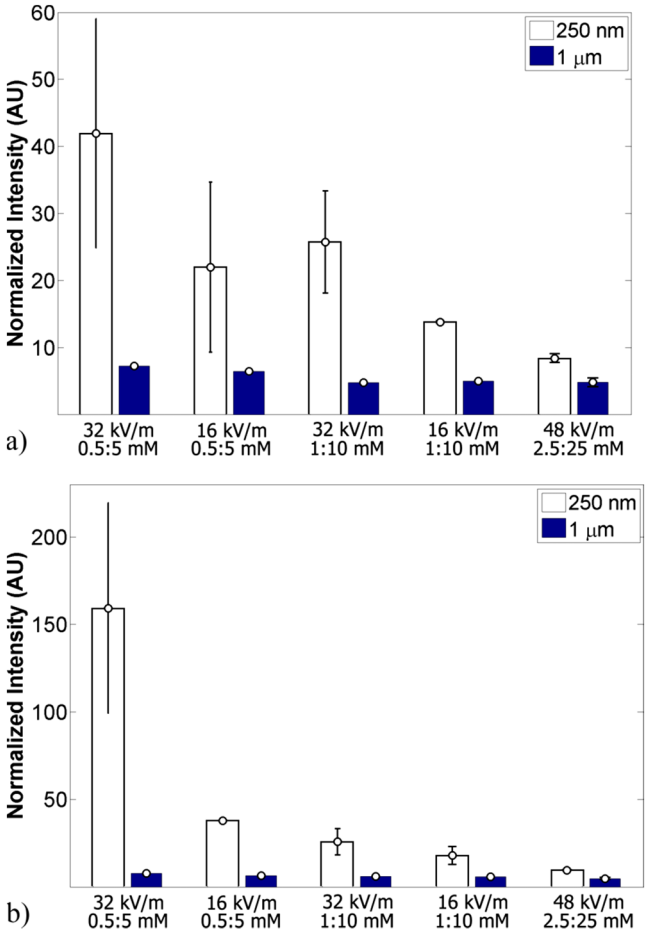

FIG. 6. (Color online) Bar graphs of experimental results comparing the concentration enhancement in a 250 nm nanochannel and a 1 μm microchannel at different buffer concentrations and electric fields. (a) Comparison of concentration enhancement 15 mm downstream of the channel. (b) Comparison of the maximum concentration enhancement observed at all detection points. The error bars indicate one standard deviation from the mean intensity value of three separate experiments for each set of conditions.

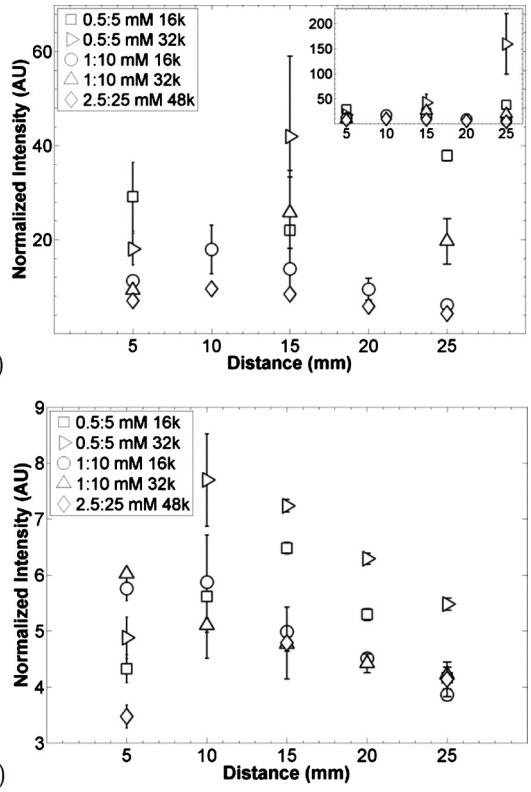

FIG. 7. Experimental results showing maximum concentration increase vs distance down channel for (a) a 250 nm deep nanochannel and (b) a 1 μm deep microchannel. Data shows all experimental conditions and error bars associated with the three realizations performed at each condition. In the nanochannel, the concentration enhancement depends on the buffer concentration and the electric field strength, whereas in the microchannel, these dependencies are much weaker. The error bars indicate one standard deviation from the mean intensity value of three separate experiments for each set of conditions.

Nernst–Planck equation implicitly assumes an ideal, dilute solution with an electrochemical potential, μ, given as[45]

$$\mu_i = kT \log(n_i) + z_i e\Phi. \tag{3}$$

In our work, we will consider three species, the positive and negative ions of a background salt solution and a charged sample species that we are interested in investigating. We consider the simple case where the sample species is dilute with respect to the salt concentration, thus the sample species is passive and does not influence the electric field.[18] This is a reasonable assumption because in all experimental cases, the sample ions are at least 100 times less concentrated than the background ion concentration. Additionally, we consider a simple salt where the only species are the positive and negative ions, thus we have n^+ and n^-. The salt is also considered to be monovalent ($z^+=1$ and $z^-=-1$) and symmetric ($D^+=D^-$). We use the superscript + and − to denote the positive and negative ions.

The electric potential is found by solving Poisson's equation

$$\varepsilon \nabla^2 \Phi = -\rho, \tag{4}$$

where ε is the permittivity of the solvent (water) and ρ is the volumetric charge density. The charge density is given simply by the sum of the ion concentrations, $\rho=e(n^+-n^-)$. In our experiments an electric field is applied down the axial length of the channel and an electric potential occurs due to the charge within the system. In such problems, it is common to decompose the electric potential into a part that arises due to free charges and the externally applied field,[46]

$$\nabla\Phi = \nabla\phi(x,y) - E(x)\mathbf{i}, \tag{5}$$

where E is the applied axial electric field, with x as the axial coordinate, and y is the distance from the centerline of the channel.

The fluid motion is determined by the Stokes equation, neglecting the fluid inertia at these extraordinarily low Reynolds numbers,

$$0 = -\nabla P + \eta\nabla^2\mathbf{u} - \rho\nabla\Phi, \tag{6}$$

with the additional constraint of incompressible flow,

$$\nabla\cdot\mathbf{u} = 0. \tag{7}$$

Here, η is the dynamic viscosity of the fluid and P is the pressure.

Downloaded 11 Mar 2011 to 209.94.128.116. Redistribution subject to AIP license or copyright; see http://pof.aip.org/about/rights_and_permissions

Equations (2), (4), (6), and (7) form a closed set of equations for the ion concentrations, electric potential, and fluid flow and comprise the classical theory for electrokinetic flow.[8,45]

B. Thin channel equations

Since experimental nanofluidic channels are typically much smaller in the depth direction than the length, the formulation can be simplified using the thin channel approximation. The procedure we follow to derive the thin channel equations is similar to the work of Lin *et al.*[32] that developed an electrokinetic flow model for shallow microchannels. We nondimensionalize equations using the following scales:

$$[x] = L_0, \quad [y] = H, \quad [\phi] = \frac{kT}{e}, \quad [u] = U_0 = \frac{\varepsilon(kT/e)E_0}{\eta},$$

$$[v] = \frac{U_0 H}{L_0}, \quad [t] = \frac{L_0}{U_0}, \quad [p] = \frac{\eta U_0 L_0}{H^2},$$

$$[n] = n_\infty, \quad [E] = E_0, \quad [\zeta] = \frac{kT}{e}.$$

Above, L_0 is the axial length scale for the channel, H is the channel half-height, E_o is the average applied field in the channel (i.e., total voltage drop divided by the channel length), n_∞ is ion number density in the supply reservoir of the low-conductivity fluid, and ζ is the zeta potential of the channel. We typically use $L_0 = 1$ mm, to easily connect to our experiments where the length of the channels are either 5 or 30 mm. We ignore the channel width and only consider the transport to be two-dimensional.

Applying these scales to our governing equations in two dimensions yields equations for salt transport of the positive ions,

$$\begin{aligned}\mathrm{Pe}\ \delta\left(\frac{\partial n^+}{\partial t} + \frac{\partial (u n^+)}{\partial x} + \frac{\partial (v n^+)}{\partial y}\right) &= \delta^2 \frac{\partial}{\partial x}\left(\frac{\partial n^+}{\partial x} + n^+ \frac{\partial \phi}{\partial x}\right) - \delta\Gamma \frac{\partial (n^+ E)}{\partial x} \\ &+ \frac{\partial}{\partial y}\left(\frac{\partial n^+}{\partial y} + n^+ \frac{\partial \phi}{\partial y}\right),\end{aligned} \tag{8}$$

negative ions,

$$\begin{aligned}\mathrm{Pe}\ \delta\left(\frac{\partial n^-}{\partial t} + \frac{\partial (u n^-)}{\partial x} + \frac{\partial (v n^-)}{\partial y}\right) &= \delta^2 \frac{\partial}{\partial x}\left(\frac{\partial n^-}{\partial x} - n^- \frac{\partial \phi}{\partial x}\right) + \delta\Gamma \frac{\partial (n^- E)}{\partial x} \\ &+ \frac{\partial}{\partial y}\left(\frac{\partial n^-}{\partial y} - n^- \frac{\partial \phi}{\partial y}\right),\end{aligned} \tag{9}$$

Poisson's equation for the electric potential,

$$\delta^2 \frac{\partial^2 \phi}{\partial x^2} + \frac{\partial^2 \phi}{\partial y^2} = -\frac{1}{2\lambda^2}(n^+ - n^-), \tag{10}$$

conservation of mass,

$$\frac{\partial u}{\partial x} + \frac{\partial v}{\partial y} = 0, \tag{11}$$

the conservation of momentum in the x-direction,

$$\begin{aligned}\frac{\partial P}{\partial x} &= \delta^2 \frac{\partial^2 u}{\partial x^2} + \frac{\partial^2 u}{\partial y^2} - \left(\delta^2 \frac{\partial^2 \phi}{\partial x^2} + \frac{\partial^2 \phi}{\partial y^2}\right)\left(E - \frac{\delta}{\Gamma}\frac{\partial \phi}{\partial x}\right) \\ &+ \delta \frac{\Gamma}{2}\frac{\partial E^2}{\partial x} - \delta^2 \frac{\partial E}{\partial x}\frac{\partial \phi}{\partial x},\end{aligned} \tag{12}$$

and y-direction,

$$\frac{\partial P}{\partial y} = \delta^4 \frac{\partial^2 v}{\partial x^2} + \delta^2 \frac{\partial^2 v}{\partial y^2} + \frac{\delta}{\Gamma}\left(\delta^2 \frac{\partial^2 \phi}{\partial x^2} + \frac{\partial^2 \phi}{\partial y^2}\right)\frac{\partial \phi}{\partial y} - \delta^2 \frac{\partial \phi}{\partial y}\frac{\partial E}{\partial x}. \tag{13}$$

Our dimensionless numbers are the dimensionless Debye length, $\lambda = \lambda_D / H$, the Peclet number, $\mathrm{Pe} = U_0 H / D$, the strength of the applied electric field relative to the electric field across the channel depth, $\Gamma = E_0 H / kT/ze$ and $\delta = H/L_0$ the ratio of channel height to length. The Debye length is defined as $\lambda_D = \sqrt{\epsilon kT / 2e^2 z^2 n_\infty}$.

The boundary conditions applied at the wall are no flux of ionic species,

$$\left(\frac{\partial n^+}{\partial y} + n^+ \frac{\partial \phi}{\partial y}\right)\Bigg|_{y=\pm 1} = 0,$$

$$\left(\frac{\partial n^-}{\partial y} - n^- \frac{\partial \phi}{\partial y}\right)\Bigg|_{y=\pm 1} = 0,$$

no-slip and no-normal flow,

$$u(y = \pm 1) = 0, \quad v(y = \pm 1) = 0,$$

and fixed potential

$$\phi(y = \pm 1) = \zeta.$$

The dimensionless diffuse layer potential, or zeta potential, ζ, is defined relative to the thermal voltage, $kT/e = 25.7$ mV at room temperature. Equivalently, the wall charge, q_w, may be specified and thus the zeta potential can be set through the Grahame equation,[47]

$$\frac{q_w}{\sqrt{n_\infty 8 \varepsilon kT}} = n_c \sinh\left(\frac{\zeta}{2}\right).$$

In our case, the wall charge was measured experimentally and the Grahame equation was found to be valid in the regime we are operating in, as discussed in Sec. II D. We will use a constant wall charge of -0.02 C/m^2 unless otherwise noted.

We now consider an expansion of these equations with δ and take the limit as δ goes to zero. For a generic function our expansion will follow $f = f_0 + \delta f_1$. In our system, $\delta = H/L_0$ is extremely small; the height of the experimental channel is 250 nm or 1 μm while the length scale is on the order of millimeters, thus we only extend our analysis to the lowest order. In what follows, we will also use the depth averaging operation defined for a generic function as

Downloaded 11 Mar 2011 to 209.94.128.116. Redistribution subject to AIP license or copyright; see http://pof.aip.org/about/rights_and_permissions

$$\bar{f} = \frac{1}{2}\int_{y=-1}^{y=1} f(y)dy.$$

1. Salt transport

Substituting the expansions into the ion transport equations yields a simple expression for the ion densities at lowest order,

$$\frac{\partial}{\partial y}\left(\frac{\partial n_0^+}{\partial y} + n_0^+\frac{\partial \phi_0}{\partial y}\right) = 0, \tag{14}$$

$$\frac{\partial}{\partial y}\left(\frac{\partial n_0^-}{\partial y} - n_0^-\frac{\partial \phi_0}{\partial y}\right) = 0. \tag{15}$$

These expressions simply state that the electrochemical potential across the channel is constant at any x-location. Solving this equation provides that the number density follows a Boltzmann distribution:

$$n_0^+ = n_c^+ e^{-(\phi_0-\phi_c)} = n_c e^{-\phi_0}, \tag{16}$$

and

$$n_0^- = n_c^- e^{(\phi_0-\phi_c)} = n_c e^{\phi_0}. \tag{17}$$

Formally, we relate the constant of integration in the Boltzmann distribution to values at the centerline, denoted by the subscript c. However, we are in the regime where the double layers are finite, but still relatively small compared to the channel (i.e., $\lambda/H < 0.1$) and the potential along the centerline of the channel is zero and $n_c^+ = n_c^- = n_c$. Assuming a local Boltzmann distribution in a channel with finite but nonoverlapped EDLs is a commonly used approximation in nanochannel work.[7,48] Accounting for finite double layers provides a formulation unique from those developed in prior FASS work in microchannels.

To close the problem, we must couple the Boltzmann distribution to Poisson's equation, which at zeroth order is

$$\lambda^2\frac{\partial^2 \phi_0}{\partial y^2} = n_c \sinh(\phi_0). \tag{18}$$

Note that the center concentration is scaled to our reference value, n_∞ which is the number density in the low-conductivity supply reservoir. In this paper, we always have concentration ratios of 10; so in this work n_c will be either 1 or 10. Note that in our scaling here, we have chosen to express our equations to have a constant characteristic Debye length based on a reference concentration and a varying centerline salt concentration.

In order to understand the dynamics in the axial direction, we must proceed to order δ in the analysis. The evolution of the positively charged species at this order is,

$$\mathrm{Pe}\left(\frac{\partial n_0^+}{\partial t} + \frac{\partial (u_0 n_0^+)}{\partial x} + \frac{\partial (v_0 n_0^+)}{\partial y}\right) = -\Gamma\frac{\partial (n_0^+ E)}{\partial x} + \frac{\partial}{\partial y}\left(\frac{\partial n_1^+}{\partial y} + n_0^+\frac{\partial \phi_1}{\partial y} + n_1^+\frac{\partial \phi_0}{\partial y}\right). \tag{19}$$

This expression can be simplified by depth averaging the above equation and applying the no flux and no normal flow boundary conditions at $y = \pm 1$,

$$\mathrm{Pe}\frac{\partial \overline{n_0^+}}{\partial t} + \mathrm{Pe}\frac{\partial (\overline{u_0 n_0^+})}{\partial x} + \Gamma\frac{\partial (\overline{n_0^+ E})}{\partial x} = 0. \tag{20}$$

Likewise we obtain the same equation for n^-,

$$\mathrm{Pe}\frac{\partial \overline{n_0^-}}{\partial t} + \mathrm{Pe}\frac{\partial (\overline{u_0 n_0^-})}{\partial x} - \Gamma\frac{\partial (\overline{n_0^- E})}{\partial x} = 0. \tag{21}$$

We rename the parameter $\Gamma/\mathrm{Pe} = b = \eta D/\varepsilon(kT/e)^2$ to remind us this is a system property that does not depend on the flow velocity or applied electric field. The parameter b is the ratio of the ion electrophoretic velocity to the channel electroosmotic velocity. For reference, the parameter $b \approx 2.5$ for common aqueous systems with simple salts. Adding and subtracting Eqs. (20) and (21), we can recast in terms of the dimensionless charge density $\rho = (n^+ - n^-)/2$ and the electrical conductivity $\sigma = (n^+ + n^-)/2$,

$$\frac{\partial \bar{\rho}_0}{\partial t} + \frac{\partial (\overline{u_0 \rho_0})}{\partial x} + b\frac{\partial (\bar{\sigma}_0 E)}{\partial x} = 0, \tag{22}$$

$$\frac{\partial \bar{\sigma}_0}{\partial t} + \frac{\partial (\overline{u_0 \sigma_0})}{\partial x} + b\frac{\partial (\bar{\rho}_0 E)}{\partial x} = 0. \tag{23}$$

From Eqs. (16) and (17), the charge density and conductivity are known locally as $\rho_0 = \sigma_c \sinh(\phi_0)$ and $\sigma_0 = \sigma_c \cosh(\phi_0)$. The centerline conductivity, σ_c, is supplied from the boundary condition at the channel entrance.

Note that for the case of constant wall charge, $\bar{\rho}$ is a constant throughout the channel and Eq. (22) reduces to the statement that the ionic current is constant,

$$\frac{\partial}{\partial x}(\overline{u_0 \rho_0} + b\bar{\sigma}_0 E) = 0. \tag{24}$$

2. Flow

Next, we turn to the flow equations and consider the conservation of momentum and mass. Depth averaging the conservation of mass at zeroth order and applying the boundary condition yields the obvious result,

$$\frac{\partial \bar{u}_0}{\partial x} = 0. \tag{25}$$

The zeroth order equation for the x momentum is,

$$\frac{\partial P_0}{\partial x} = \frac{\partial^2 u_0}{\partial y^2} - \frac{\partial^2 \phi_0}{\partial y^2}E, \tag{26}$$

and the y momentum equation yields

$$\frac{\partial P_0}{\partial y} = 0. \tag{27}$$

Since the pressure is constant across the channel depth, we can express the pressure gradient as dP/dx; pressure is

Downloaded 11 Mar 2011 to 209.94.128.116. Redistribution subject to AIP license or copyright; see http://pof.aip.org/about/rights_and_permissions

only a function of x. We can now easily integrate the x-momentum equation with no-slip boundary conditions to obtain,

$$u_0(x,y) = -E\zeta\left(1 - \frac{\phi_0(y)}{\zeta}\right) - \frac{dP}{dx}\frac{1-y^2}{2}. \tag{28}$$

The above expression for the velocity can be found in many previous papers on nanochannel flow.[49,50] For convenience, we define the function $\Psi(y)$ as

$$\Psi(y) = \left(1 - \frac{\phi_0(y)}{\zeta}\right), \tag{29}$$

which simply becomes $\Psi = 1$ in the thin EDL limit. Depth averaging yields the local average flow velocity, $\bar{u}$,

$$\bar{u}_0 = -E\zeta\bar{\Psi} - \frac{dP}{dx}\frac{1}{3}. \tag{30}$$

In the final expression we must remember that E, ζ, $\bar{\Psi}$, and dP/dx are functions of x. Note that in our system the zeta potential is negative and thus the flow is positive for a positive electric field. This expression is the same in the microchannel limit where $\bar{\Psi} \to 1$.

3. Sample transport

Following the same procedure as the salt transport, we can find the zeroth order equation for the evolution of the sample species. Since we are assuming a species concentration low enough that it only acts as a passive tracer and does not impact the charge density or conductivity, at the zeroth order, the sample species satisfies,

$$\frac{\partial}{\partial y}\left(\frac{\partial n_0^s}{\partial y} + z_s n_0^s \frac{\partial \phi_0}{\partial y}\right) = 0, \tag{31}$$

where the superscript s denotes the sample from the positive and negative ionic species. Thus, the sample species is in local chemical equilibrium across the channel's depth,

$$n_0^s = n_c^s e^{-\phi_0 z_s}. \tag{32}$$

In our experiments, we will consider the sample species is negatively charged and has a valence of $z_s = -1.75$, as discussed in Sec. II D. The sample species are strongly repelled from the walls.

To understand the dynamics of the sample species, we proceed to the next order in δ as before to obtain,

$$\mathrm{Pe}_s\frac{\partial \overline{n_0^s}}{\partial t} + \mathrm{Pe}_s\frac{\partial(\overline{u_0 n_0^s})}{\partial x} + \Gamma_s\frac{\partial(\overline{n_0^s}E)}{\partial x} = 0. \tag{33}$$

The mobility and charge of the sample species are typically different than the background salt and thus the Peclet number and Γ are appropriately defined. We can rewrite this transport equation as

$$\frac{\partial \overline{n_0^s}}{\partial t} + \frac{\partial}{\partial x}(\overline{u_0 n_0^s} + b_s\overline{n_0^s}E) = 0. \tag{34}$$

C. Model summary

Our system of equations is relatively simple. Here, and for the remainder of the paper we drop the subscript 0 as we will not proceed to higher order analysis. Our formulation describes the evolution of fluid conductivity, σ, charge density ρ, and the concentration of the sample ions n_s. The axial transport is summarized from Sec. III as

$$\frac{\partial \bar{u}}{\partial x} = 0, \tag{35}$$

$$\frac{\partial \bar{j}_\rho}{\partial x} = 0, \tag{36}$$

$$\frac{\partial \bar{\sigma}}{\partial t} + \frac{\partial \bar{j}_\sigma}{\partial x} = 0, \tag{37}$$

$$\frac{\partial \bar{n}_s}{\partial t} + \frac{\partial \bar{j}_n}{\partial x} = 0, \tag{38}$$

where the fluxes are

$$\bar{j}_\sigma = \overline{u\sigma} + b\bar{\rho}E, \tag{39}$$

$$\bar{j}_\rho = \overline{u\rho} + b\bar{\sigma}E, \tag{40}$$

$$\bar{j}_n = \overline{un_s} + b_s\bar{n}_s E. \tag{41}$$

Across the channel, $\phi(y)$ is known from numerical solution of Eq. (18) with the boundary condition of constant charge at the walls. The other variables are defined simply as $\sigma = \sigma_c \cosh(\phi)$, $\rho = \sigma_c \sinh(\phi)$, and $n = n_{c,s}e^{-z_s\phi}$. The flow field is known as

$$u(y) = -E\zeta\Psi(y) - \frac{dP}{dx}\frac{1-y^2}{2}. \tag{42}$$

All of these values can be depth averaged via simple numerical integration. In the x-direction, the total voltage and pressure drops are known as well as the concentrations at the channel inlet, which provide the axial boundary conditions for the model.

In the limit of thin double layers the bulk fluid is electroneutral and the ionic current is only composed of the Ohmic piece, $j_\rho = bE\sigma$, the conductivity flux reduces to $j_\sigma = \bar{u}\sigma$, and the sample species flux becomes $j_n = \bar{u}n_s + bEn_s$. This simple thin EDL model is the basis for all previous work on FASS.[17]

Whether we are in the thin EDL limit or not can be determined by the Dukhin number (Du), which traditionally compares the surface conduction to bulk ion conduction. The Dukhin number has been used in other nanochannel work as a critical parameter to characterize the system behavior.[38,39] In our formulation, the Dukhin number is equivalent to the ratio of the two terms that comprise the ionic current; $\mathrm{Du} = \overline{u\rho}/b\bar{\sigma}E$. For a channel of uniform composition this value can be readily estimated. Since the average charge density is related to the electric field at the wall via the dimensionless Poisson equation, $\bar{\rho} = \lambda^2 \partial\phi/\partial y|_{y=1}$, we estimate that $\bar{\rho} \sim \zeta\lambda$.

Downloaded 11 Mar 2011 to 209.94.128.116. Redistribution subject to AIP license or copyright; see http://pof.aip.org/about/rights_and_permissions

The average velocity is estimated as $u_0 \sim \zeta(1-\lambda)$, where we simply remove a stagnant layer of the size of λ from the otherwise flat electro-osmotic flow profile. For the bulk conduction, $E=1$ for a uniform channel by definition and b is a property of the fluid and ion system. Near the wall, $\rho \sim \sigma$ since the number of counterions far exceeds the number of coions at our ζ potentials. Thus we can make the estimate that $\bar{\sigma} \sim 1+2(\bar{\rho}-\lambda)$. Putting our estimates together yields,

$$\mathrm{Du} = \frac{\zeta^2 \lambda(1-\lambda)}{b[1+2\lambda(\zeta-1)]}.$$

This simple estimate matches the calculated ratio of the terms in the current very well. For cases of small Dukhin number, we expect that the classic microchannel model would be quite adequate.

Note that our simple model stated above ignores molecular diffusion and dispersion caused by the nonuniform velocity field in the y-direction. Given the diffusivity of common salts ($\sim 10^{-9}$ m^2/s) and the time scale for the experiments (~ 10 s), the diffusion length scale is about 100 μm. Therefore, because the experimental channel lengths are 30 mm long, ignoring axial diffusion seems a reasonable first approximation. Although this may not be true in practice, it will give us the insight we need to qualitatively explain the phenomena observed. We revisit diffusion in Sec. VI C, which will allow for a better comparison between experiment and theory.

V. SOLUTION FOR A SINGLE CHANNEL

For simplicity and to elucidate the basic mechanisms, we first consider FASS in a single channel with a known applied pressure and voltage difference across the channel, ΔP and ΔV. In this solution to the model equations, we assume that there are different regions in the system where all fluid properties are constant over a long region and that the interface between the each region is sharp. For this work, we assume there is initially a region of high conductivity (region 1) surrounding a region of low conductivity (region 2) as shown in Fig. 1(b).

We can use current and mass continuity to calculate the voltage and pressure drop across each region. The total voltage and pressure drops across each region must equal the known applied voltage and pressure for the channel. The calculation is somewhat more complicated than the microchannel case where the electrical problem and flow problem decouple. For the sharp interface assumption, we find that there exist a set of jump conditions for the propagation of the interfaces. This sharp interface assumption allows us to easily compute the speed of propagation of the interfaces between different regions in the system and fully describe the dynamics. There is no need to solve the complete partial differential equations.

A. Mean flow

The average velocity, $\bar{u}$ must be the same at all x locations due to incompressibility. Integrating the equation for the mean flow, Eq. (30), over a length of the channel, L_1, we obtain,

$$\bar{u} = -\frac{1}{L_1}\int_0^L E\zeta\bar{\Psi}dx + \frac{\Delta P_1}{3L_1}, \tag{43}$$

where ΔP_1 is the total pressure drop (inlet pressure minus outlet pressure) across the length of channel. Over a region of the channel, where the fluid has constant composition, the above expression simplifies to

$$\bar{u} = -\frac{\Delta V_1 \zeta\bar{\Psi}}{L_1} + \frac{\Delta P_1}{3L_1}, \tag{44}$$

where ΔV_1 is the total voltage drop across this length of channel.

B. Ionic current

The ionic current, j_ρ, can be written as the sum of a component due to the electric field and one due to the pressure gradient,

$$j_\rho(y) = E[-\zeta\Psi(y)\rho(y) + b\sigma] - \frac{dP}{dx}\rho(y)\frac{1-y^2}{2}. \tag{45}$$

Depth averaging, this expression results in

$$\bar{j}_\rho = E[-\zeta\overline{\Psi\rho} + b\bar{\sigma}] - \frac{dP}{dx}\overline{\rho\frac{(1-y^2)}{2}}. \tag{46}$$

Integrating this expression over a length of channel, L_1, where the fluid has constant composition, the above expression simplifies to

$$\bar{j}_\rho L_1 = \Delta V_1[-\zeta(\overline{\Psi\rho}) + b\bar{\sigma}] + \Delta P_1\overline{\frac{\rho(1-y^2)}{2}}, \tag{47}$$

which we write in shorthand as

$$\bar{j}_\rho = \frac{\Delta V_1}{R_1} + \frac{\Delta P_1}{R_{h,1}}. \tag{48}$$

In the thin double layer limit, $R_{h,1} \to \infty$ and $R_1 \to L_1/b\sigma$ and thus we recover Ohm's law.

C. Total pressure and voltage drop

The mean flow in the regions of high and low conductivity (regions 1 and 2) must be equal, therefore from Eq. (44),

$$-\Delta V_1\frac{\zeta_1\bar{\Psi}_1}{L_1} + \frac{\Delta P_1}{3L_1} = -\Delta V_2\frac{\zeta_2\bar{\Psi}_2}{L_2} + \frac{\Delta P_2}{3L_2}. \tag{49}$$

The ionic current in the two regions must also be equal, therefore from Eq. (48),

$$\frac{\Delta V_1}{R_1} + \frac{\Delta P_1}{R_{h,1}} = \frac{\Delta V_2}{R_2} + \frac{\Delta P_2}{R_{h,2}}. \tag{50}$$

The total voltage drop across the channel is known, $\Delta V_1 + \Delta V_2 = \Delta V$, as well as the total pressure drop, $\Delta P_1 + \Delta P_2 = \Delta P$. The total applied voltage is the dimensionless channel length, $\Delta V = L_{\mathrm{ch}}/L_0$, by the definition of the scale for the electric field. As mentioned previously, we typically use $L_0 = 1$ mm, although this choice is arbitrary. The final result

Downloaded 11 Mar 2011 to 209.94.128.116. Redistribution subject to AIP license or copyright; see http://pof.aip.org/about/rights_and_permissions

is that we have four equations to solve for two unknown voltage drops and two unknown pressure drops. Since regions 1 and 2 are constant in composition, the electric field and pressure gradient are readily computed as constants that are different in the two regimes.

D. Interface jump conditions

Once the pressure and voltage drop across each region is known, then the fluxes are straightforward to evaluate since the fluxes depend on the electric field and pressure gradient. The fluid's electrical conductivity is advected down the channel according to Eq. (37). Applying this equation across a jump where there are two regions of constant conductivity (1 and 2), allows us to show that the position of the interface propagates at a speed U_σ,

$$U_\sigma = \frac{\bar{j}_{\sigma,1} - \bar{j}_{\sigma,2}}{\bar{\sigma}_1 - \bar{\sigma}_2}. \tag{51}$$

Applying Eq. (38) across a region where there are sample ions on one side and no sample ions on the other in a region of constant background fluid shows that the interface propagates as

$$U_s = \frac{\bar{j}_n}{\bar{n}_s}. \tag{52}$$

We can also look at what happens to the sample concentration across an interface where the conductivity changes. It is straightforward to show that the enhancement in sample concentration is given as

$$\frac{n_{s,1}}{n_{s,2}} = \frac{U_{s,2} - U_\sigma}{U_{s,1} - U_\sigma}. \tag{53}$$

In the limit of thin double layers we recover the fact that the interfaces propagate as $U_\sigma \to \bar{u}$ and $U_s \to \bar{u} + bE$. In this limit, we also obtain $\sigma_1 E_1 = \sigma_2 E_2$ from current continuity. The enhancement of the sample species simplifies to

$$\frac{n_{s,1}}{n_{s,2}} = \frac{\bar{u} + bE_2 - \bar{u}}{\bar{u} + bE_1 - \bar{u}} = \frac{E_2}{E_1} = \frac{\sigma_1}{\sigma_2}. \tag{54}$$

Thus our model recovers the classic microchannel FASS model in the thin EDL limit.[17] We emphasize the simplicity of what becomes a set of velocities that can be used to draw straight characteristic lines for the location of the different interfaces.

VI. MODEL RESULTS

In this section, we describe the use of the model solution to explain experimental observations. We start with the simple single-channel model presented in Sec. V. In a simple application of the model, we assume that the applied pressure difference is zero and voltage across the channel is held fixed in time. We consider the solution is valid up to the time the low-conductivity region starts to leave the channel. This model has the advantage that it is simple to implement and makes predictions that are in good agreement with experimental trends. This single-channel model is only a model for the injection stage of the process that was described in Sec. II F and an assumption of the initial condition for the channel contents must be made. The injection stage is the one in which the sample stacking occurs. This single-channel model is capable of explaining key experimental trends, however some aspects of the experiments cannot be obtained without extending this model to account for the inlet channels of the complete geometry. Thus, in Sec. VI B, we extend our single-channel model to account for the inlet channels that allow us to compute critical dynamics, most importantly the amount of sample and low-conductivity fluid injected into the channel during the gating step.

A. Single-channel results

Figure 8(a) shows key features of the model in a schematic diagram. We assume an initial conductivity distribution as shown the Fig. 8(a) where the low-conductivity region is the middle 5 mm of a 30 mm channel. The low-conductivity region contains the sample ions at a charge of $z=-1.75$ (for fluorescein). Figure 8(a) shows the electric potential, sample ion distributions, and velocity profiles across the channel depth. We notice that the electric double layer is finite, leading to nonuniform distributions in electric potential. These nonuniform distributions cause the sample ions to prefer the center of the channel, since the sample ions are negatively charged and repelled from the walls. Additionally, the velocity is nonuniform. The coupled effect of nonuniform velocity and nonuniform sample distribution leads to significant deviation from the transport of ions in a microchannel.[7]

In the low-conductivity region, the electric field is high and thus the electro-osmotic flow is greater than in the high-conductivity buffer region. An internally generated pressure gradient in the low-conductivity region opposes the electro-osmotic flow in order to obey mass conservation. The velocity along the centerline is actually negative in this case while the mean flow is positive. Since the electric double layer is thick, the sample ions prefer the center of the channel and thus the flow component of the sample ion flux is *less* than would be predicted in the thin double layer limit where the ions are subject to the mean flow, i.e., $\overline{un_s}/\bar{n}_s < \bar{u}$. In the high-conductivity buffer region, the situation is reversed. The electro-osmotic flow is slower and thus the internally generated pressure gradient enhances the flow. The centerline velocity in this region is *greater* than the mean flow. Again the sample ions are repelled from the wall and thus the flow component of the sample ion flux is greater than mean flow, i.e., $\overline{un_s}/\bar{n}_s > \bar{u}$. This effect is schematically shown in Fig. 8(a). The full velocity field in both regions is shown as the solid curved line. The mean fluid velocity, $\bar{u}$, is shown as the dashed line and the mean sample velocity, $\overline{un_s}/\bar{n}_s$, is shown as the vertical solid line. In a microchannel, sample ions can occupy any cross stream location in the channel and sample ion flux due to fluid flow is equal to the mean flow in both regions. In a nanochannel since the center location is preferred, the sample flux due to fluid flow differs from the mean flow.

The subtle difference between the mean sample velocity due to the flow, $\overline{un_s}/\bar{n}_s$, and the mean flow velocity, $\bar{u}$, leads

Downloaded 11 Mar 2011 to 209.94.128.116. Redistribution subject to AIP license or copyright; see http://pof.aip.org/about/rights_and_permissions

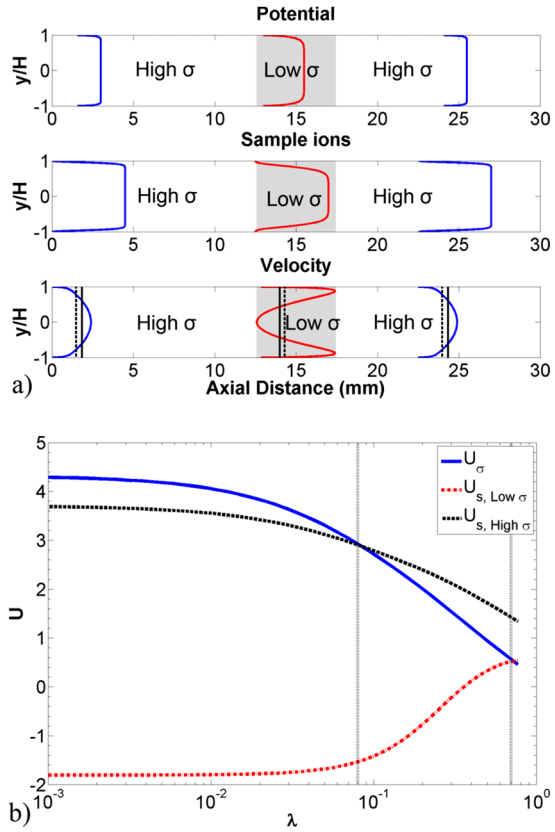

FIG. 8. (Color online) (a) Schematic of the electric potential, sample ion distribution, and velocity profiles across the depth of the channel, y. We show profiles for the high-conductivity (unshaded) and low-conductivity (shaded) regions. The parameters correspond to the 1 to 10 mM concentration ratio in a 250 nm channel. In the velocity figure, the dashed vertical line shows mean flow that is constant at any x location. The solid vertical lines show the depth average flux of sample ions due to the flow, $\overline{un_s}/\overline{n}_s$. In a microchannel, the two velocities are the same. (b) The speed of propagation of the conductivity interface, the speed of the sample ions in the high-conductivity region, and the speed of the sample ions in the low-conductivity region, as a function of the dimensionless Debye length λ. In this figure we fix the concentrations ration at 1 to 10 mM but varying channel height. Between $0.7>\lambda>0.08$ (in this particular case), the sample ions in the trailing high-conductivity region move faster than the interface, thus any sample ions in this regime would catch up to the trailing edge of the low-conductivity plug. Ions in the low-conductivity region move slower than the interface and thus move out of the region from the trailing edge. Sample ions approach the trailing edge of the low-conductivity interface from both sides, leading to focusing.

to the quite different behavior in the nanochannels. When the situation is extreme, the sample velocity in the low- and high-conductivity regions can be such that it is possible to *focus* the entirety of the sample ions at the trailing interface between the high- and low-conductivity regions. In Fig. 8(b), we plot the velocity of the interface between high and low conductivity (in solid blue), the velocity of the sample ions in the trailing high-conductivity buffer (in dotted black), and the velocity of the sample ions in the low-conductivity buffer (in dashed red). We keep the concentration ratio fixed at 1 to 10 mM, but vary the channel height. We notice that for very thin double layer thicknesses, the interface velocity is faster than the sample ions in both the high- and low-conductivity regions. In the frame of the trailing edge of the conductivity interface, sample ions in the low-conductivity region approach the interface, pass through, and continue out the other side with a slower velocity (leading to stacking). This is the regime typically described in microchannel FASS. Focusing of the sample ions in this particular case sets in at a double layer thickness of about $\lambda=0.08$, where the sample ion velocity in the high-conductivity region becomes faster than the conductivity interface. When λ is in the range $0.08<\lambda<0.7$, sample ions in the low-conductivity region move with negative velocity (in the frame moving with the conductivity interface) and thus want to leave the low-conductivity region from the trailing edge. However, sample ions in the trailing high-conductivity buffer would approach the conductivity interface from the other direction. Sample ions in either region would approach the trailing edge of the low/high conductivity regions, leading to focusing. Therefore, in a nanochannel with finite double layers, the ions repelled from the walls *coupled to the induced pressure gradients* leads to a focusing effect. This novel effect cannot be found in microchannels and relies on the device dimensions being small enough that the EDLs have finite size compared to the channel half-height. This focusing of sample ions theoretically leads to infinite concentration enhancement. Of course, molecular diffusion will prevent such infinite concentration enhancement (as we will consider in Sec. VI C).

Continuing to increase the double layer thickness, the interface velocity decreases as the double layer thickens. As the double layer gets larger, $\lambda>0.7$, the sample ion velocity in the low-conductivity region increases to the point where ions would leave the low-conductivity region from the front, leading to destacking, since ions in both cases will want to propagate faster than the interface. This destacking effect is mainly due to the fact that as the double layers get thicker the concentration ratio needed for efficient stacking is lost. While our model predicts destacking at thick double layers, experimentally we are currently unable to probe this regime of parameter space.

We now use our 1D model to compute the characteristics of the solution. In our simple model, the solution consists of nothing more than computing the velocity of propagation of the leading and trailing edge of the low-conductivity region using Eq. (51), the velocity of propagation of the leading and trailing edge of the sample ions using Eq. (52) and the enhancement ratio using Eq. (53). An example solution is shown in Fig. 9 where we compare the solution in a 250 nm and 1 μm channel, respectively. In this case, we have matched experimental conditions with data shown in Fig. 5. Here we have assumed the channel to be 30 mm and the sample region to be 5 mm. The low-conductivity region and the initial location of the sample ions are matched in this example, corresponding to 5 mm at time $t=0$. The initial concentration is taken to be 1 and 10 mM in the two regions, respectively. The red solid lines on the figure correspond to the leading and trailing edge of the sample, and the dashed blue lines correspond to the leading edge and trailing edge of the low-conductivity region. The axes are dimensionless using $L_0=1$ mm so an easy connection to the experiments may be made. The vertical axis is dimensionless and the conversion to seconds depends upon the applied electric field.

In both examples, we see the low-conductivity region

Downloaded 11 Mar 2011 to 209.94.128.116. Redistribution subject to AIP license or copyright; see http://pof.aip.org/about/rights_and_permissions

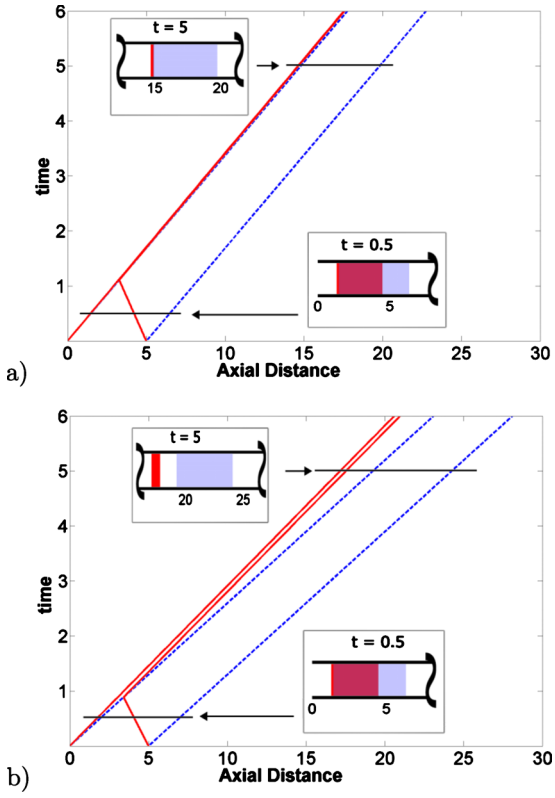

FIG. 9. (Color online) Characteristic solutions for the propagation in a single channel with two conductivity regions. In (a), we show the solution for 250 nm channel with a 1 to 10 mM concentration ratio. In (b), we have the same conditions only the channel is 1 μm deep. The x-axis is showing the distance of the channel and the y-axis is showing time. At time $t=0$, the low-conductivity region (between the two dashed lines), is between $x=0$ and 5, and the sample (between the two solid lines) is also between $x=0$ and 5, in both cases. However, as time progresses, the low-conductivity region and the sample propagate differently. Graphically we see that the space between the two solid lines after the sample exits the low-conductivity region is compressed significantly in the nanochannel, indicating a much high concentration enhancement. The axis are dimensionless using $L_0=1$ mm and $t_0=L_0/U_0$. The solution in dimensionless terms does not depend upon the electric field.

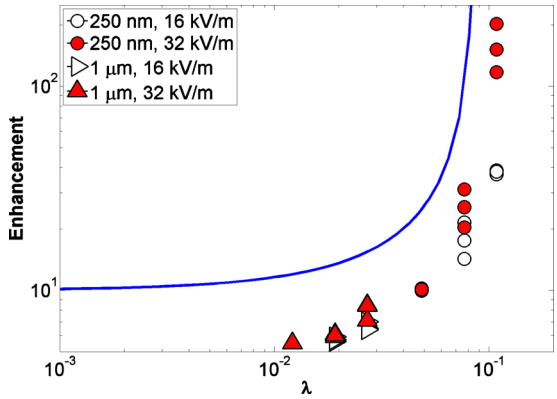

FIG. 10. (Color online) Maximum theoretical concentration enhancement ratio as a function of Debye length for a 5 mm long plug in a 30 mm straight channel, plotted along with experimental data. In this figure the Debye length is defined for the low-conductivity region and the conductivity ratio is 10 to 1. For this calculation, the concentrations are held fixed at 1 and 10 mM and the channel height is varied. The 250 nm data are shown as circles and the 1 μm channel data are shown as triangles. The experimental data are below the theoretical maximum due to diffusion and other inaccuracies associated with gating and plug length, however the trend is in good agreement with the data. The open shapes are the lower electric field (16 kV/m) and the filled points are for the higher electric fields (32 kV/m).

propagate down the channel with constant speed, although the region moves slower in the nanochannel because finite double layers cause a lower mean velocity.[7] Furthermore, in both examples, the leading edge of the sample ions inside the low-conductivity region initially travels with negative velocity and moves out of the low-conductivity region through its trailing edge. Once in the high-conductivity buffer, the leading and trailing edge of the sample travel at the same speed (solid lines after $t=1$) indicating that the concentration will no longer change after this time. However the trailing edge of the sample and the conductivity interface travel at nearly the same speed in the 250 nm example while in the 1 μm example the sample travels at a slower speed. It is the speed of the sample relative to the speed of the interface that determines the amount of concentration enhancement. When the speed of the sample ions in the high-conductivity buffer is faster than the speed of the conductivity interface propagates, then focusing occurs. For the example shown, we calculate that the maximum theoretical enhancement in the 250 nm channel to be 125 and the maximum in the 1 μm channel is 13. We can see the enhancement in the nanochannel graphically by the fact that the spacing between the leading and trailing edge of the sample is drastically reduced once the sample ions leave the low-conductivity region. In the thin EDL limit, the enhancement would be 10 (set by the conductivity ratio), regardless of the other parameters. Consistent with the experimental observations, the nanochannel shows significantly higher enhancement in sample concentration.

One interesting aspect of this model is that there are limited free parameters and the result is very general. Parameters b, b_s, and z_s are essentially properties of the chosen fluid and ion system and thus are system parameters. The solution does depend upon the ζ potential or the surface charge that can be modified through surface treatments. However, once a fluid and channel system are chosen, the only controllable variable within a set of experiments is the initial size of the sample.

Using this model, in Fig. 10, we show the maximum possible concentration enhancement as a function of the dimensionless Debye length. Again, we assume an initial low conductivity and sample region of 5 mm in a 30 mm channel. Our experimental data are overlayed on the model solution, showing good agreement with the predicted trend. The experimental data are consistently below the theoretical maximum, due to lack of diffusion in the simple model and the fact that our closest detection point in the experiment is 5 mm downstream from the channel intersection. The experimental data show more enhancement at high electric fields. Although not captured by the model as currently presented, this effect can simply be understood that the concentration enhancement time scales are faster and thus diffusion has less time to ameliorate the sharpness of the peaks.

In summary, this single-channel solution predicts the correct trend for the observed increase of sample enhance-

Downloaded 11 Mar 2011 to 209.94.128.116. Redistribution subject to AIP license or copyright; see http://pof.aip.org/about/rights_and_permissions

ment in a nanochannel versus microchannel. Our simplistic model makes two predictions that are in agreement with experimental data; (1) in nanochannels the amount of enhancement is dependent on the absolute concentration of the background electrolyte with dilute solution showing stronger enhancements. This effect is due to the finite double layer effect and is contrary to the thin EDL (in microchannels) limit in where the amount of enhancement does not depend on the background concentration. (2) Increased concentration enhancement can occur in nanochannels due to focusing caused by the double layer, whereas in microchannels the maximum theoretical enhancement is limited by the conductivity ratio, 10 in our case. This simple model is useful as the end result is essentially algebraic; there is no need to solve the governing partial differential equation. The actual quantitative predictions for concentration enhancement are currently too high because not only we have not taken into account the correct electric fields within the channel, but we also did not account for diffusion. Now we will suggest a more complicated model that takes into account the four-channel geometries and moves us toward quantitative agreement.

B. Four-channel results

The primary dynamics of stacking and a qualitative interpretation of experimental results can be understood from the single-channel model of Sec. V. However, in order to make more accurate comparisons to the experiment, we must consider the constraints and dynamics imposed by the total geometry. The four-channel geometry is critical to understanding the initial condition for the injection step. We must consider the entire loading, gating, and injection sequence to fully understand our data and to know what ions are in the channels at any given time. Experimentally, only the voltage and current at the reservoirs can be controlled so we must solve for the pressure and voltage at the intersection. Once the condition at the intersection is known, the problem consists of four coupled single-channel solutions. Each channel is connected to the others through compatibility conditions at the intersection.

For our chip geometry, the pressure is held atmospheric in the reservoirs such that the total pressure drop across all four channels is the same. Due to conservation of mass at the node, the sum of the average flow rates must sum to zero,

$$0 = \sum_k \bar{u}_k = \sum_k \bar{u}_{eo,k} + \frac{\Delta P}{3} \sum_i \frac{1}{L_k}, \tag{55}$$

where $\bar{u}_{eo} = -(1/L)\int_0^L E\zeta\bar{\Psi}dx$ is the average electro-osmotic velocity over the channel length. Here the summation and subscript k denote the four channels. Solving for the pressure drop (which is the same for all four channels) yields,

$$\frac{\Delta P}{3} = \frac{\sum_k \bar{u}_{eo,k}}{\sum_i \frac{1}{L_k}}, \tag{56}$$

which provides the relationship for the mean flow,

$$\bar{u} = \bar{u}_{eo} + \frac{\sum_i \bar{u}_{eo,i}}{L\sum_k \frac{1}{L_k}}. \tag{57}$$

The current density into the channel intersection must sum to zero, i.e., $\Sigma_k j_{\rho,k} = 0$. The voltage at the center point, V_c, of the cross is given based on the controlled voltages, V_k, at the exterior of the channel,

$$V_c = \frac{\sum_k \frac{V_k}{R_k}}{\sum_k \frac{1}{R_k}} + \frac{\sum_k \overline{u_k} \frac{R_{h,k}}{R_k}}{\sum_k \frac{1}{R_k}}. \tag{58}$$

While the solution to these coupled flow and current equations cannot be written in a simple compact form, it is straightforward to compute the pressure and voltage at the center of four channels using these coupled algebraic equations.

Once the center node pressure and voltage are known, we can easily proceed in the same manner as the single-channel model. However, the sample and low-conductivity regions do not necessarily propagate along straight lines since the composition of the channel and the center voltage changes during the gating operation. We therefore must integrate the position of the interface of the two regions of conductivity and the leading and trailing edge of the sample. The result is still a straightforward model of FASS dynamics.

Referring back to Fig. 9, we recall that our single-channel model predicts the location of the interfaces of the sample ions and the high/low conductivity regions. To compare our model predictions to the experimental data, we extract the time that three of the key features pass by the measured locations. The leading and trailing edge of the sample region are the times that the leftmost and rightmost part of the fluorescent signal passes a particular x-location (see experimental data in Fig. 5). The trailing edge of the low-conductivity region is found from the time where the signal changes dramatically from a relatively low value to a high value. The conductivity interface cannot be seen after the sample ions are fully cleared from the low-conductivity region.

In Fig. 11, we compare the model predictions (lines) to the experimental observations (points). Here we see an excellent agreement between the experiment and model in terms of the timings of the primary features during the concentration enhancement process. In order to connect Fig. 11 to the raw data plots shown in Fig. 9, one must draw a vertical line at the measurement location. If the sample ions have left the low-conductivity region at this location, then we would predict a single high intensity and narrow peak. If the sample ions have not fully cleared the low-conductivity region, we would expect to see a low intensity signal followed by a high intensity peak. For example, at the 5 mm location in Fig. 11(a), we predict that a signal would emerge at 5.3 s, hold constant at a normalized intensity of 1, and then suddenly increase at 8.6 s to show a high intensity

Downloaded 11 Mar 2011 to 209.94.128.116. Redistribution subject to AIP license or copyright; see http://pof.aip.org/about/rights_and_permissions

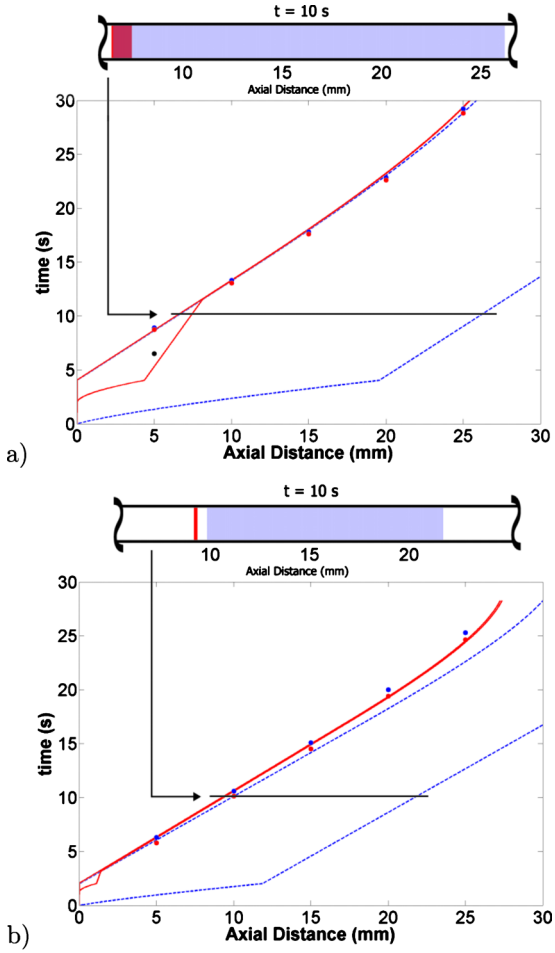

FIG. 11. (Color online) The propagation of the low-conductivity region and the sample in the four-channel arrangement using the experimental gating and injection voltages. In both figures the dashed lines denote the location of the low-conductivity region and the red solid lines denote the location of the sample ions. In a) we compared our model to experimental data in the 250 nm channel at 1 and 10 mM with an electric field of 16 kV/m. In (b), we show data for the 1 μ channel at the same concentration and electric field. The gating times are taken from the experiment (4 and 2 s, respectively) and the surface charge that bests fits the data are q_w=−0.0165 C/m^2 and q_w=−0.020 C/m^2, respectively. The horizontal line shows a schematic of the sample ion concentration and fluid electrical conductivity at a single instant in time.

narrow signal. This is precisely what is observed. In this figure, the surface charge is adjusted to provide a good fit to the data. For the 250 nm channel, the surface charge is q_w=−.0165 C/m^2, and for the 1 μm deep channel, the surface charge is q_w=−.02 C/m^2. These values are consistent with what we have measured in similar channels, described in Sec. II D.

Looking at the model results, we observe a few other important features that are consistent with our experiments. First, when the gating voltage is applied (time=0 in our plots), the sample does not immediately start flowing into the measurement channel while the low-conductivity fluid starts to flow immediately. The reason is because at the instant that the gating voltages are applied, the electric field in the exit (East) channel is such that the sample ions cannot enter this channel since they have an absolute negative velocity. Initially the electrophoretic velocity is greater than the electroosmotic flow in the East channel. The ions are forced down the south channel, as is observed experimentally and shown in Fig. 4. As low-conductivity fluid flows into the exit channel, the total electrical resistance of this channel increases and thus changes the electric field and the flow in this channel. Eventually a state is reached where the sample ions flow into the exit channel. This effect is seen in Fig. 11(a) where the sample ions do not flow until about 2 s into the applied gating voltages that last for 4 s (i.e., the red solid line is at 0 until $t \sim 2$ s, and the rapid change in slope indicates that the gating voltage has been switched to injection voltages). When the injection voltages are applied at 4 s in Fig. 11(a), the sample ions extend 4.5 mm into the channel, while the low-conductivity fluid extends 20 mm into the 30 mm channel. The location of the low-conductivity fluid and the sample ions is different than was assumed in the simple single-channel model where we assumed the sample ions and low-conductivity fluid were colocated.

While the gating time is carefully controlled, we observed experimentally that the switching from sample ions flowing in the south channel to the exit channel shows some irregularity. Therefore, it seems possible that at this junction the simple 1D model does not apply well and there may be some sensitivity to the details at the cross junction. In fact, it is important to note that our comparisons to the experiment are quite sensitive to details of the gating process, and this is an avenue for further research. Given the high voltages during the gating process, a small amount of uncertainty can impact the result as to how much sample is actually injected into the channel. This uncertainty makes exact comparisons between model and experiment challenging; however. the trends between the model and experiment appear quite accurate. We observed in the experiments that the sample ions flow into the east channel sooner in the 1 μm channel, while our model predicts they should start to flow at the same time in the two channels. This discrepancy is currently an open question.

C. Role of diffusion

In order to make a more direct comparison to the concentration enhancement data of Fig. 5 we need to account for diffusion of the sample as it is transported down the channel. Clearly, predictions of infinite sample concentration are unrealistic in the face of molecular diffusion. Formally, an analysis of this kind requires the next order of δ in our thin channel expansion. However, using classic Taylor dispersion theory we know that dispersion terms disappear as the Peclet number goes to zero,[51] which is the case when the channel heights are very small. Furthermore, previous work on electrokinetic flows in microchannels shows that dispersion (both analytically and through numerical experiments) disappears as the channels become thinner.[32] Thus, given the extreme ratio of the channel height to length, as a first approximation we neglect dispersion and add axial diffusion in a heuristic manner. Expanding our analysis to account for dispersion formally in nanochannels flows is a topic for future work. For this work, we now consider the sample ions to follow:

Downloaded 11 Mar 2011 to 209.94.128.116. Redistribution subject to AIP license or copyright; see http://pof.aip.org/about/rights_and_permissions

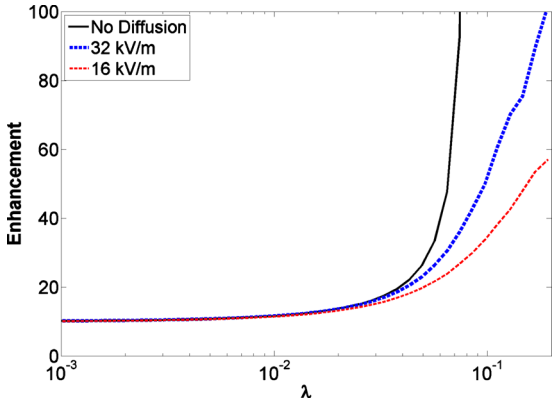

FIG. 12. (Color online) Maximum theoretical concentration enhancement ratio as a function of dimensionless Debye length, where $\lambda=\lambda_D/H$, for a 5 unit long plug length. In this figure the Debye length is defined for the low-conductivity region. For this calculation, the concentrations are held fixed at 1 and 10 mM and the channel height is varied. The behavior changes minimally if the channel height is fixed and the concentrations are varied; slight differences are due to changes in the zeta potential. The dashed lines correspond to a particular Peclet number selected to match the 16 and 32 kV/m experimental data.

$$\frac{\partial \bar{n}_s}{\partial t}+\frac{\partial}{\partial x}(\overline{un_s}+b_s\bar{n}_sE)=\frac{\delta}{\mathrm{Pe}}\frac{\partial^2\bar{n}_s}{\partial x^2}. \tag{59}$$

In this diffusive model, we propagate the interface between the high- and low-conductivity regions according to the zeroth order model (assuming the interface to be sharp) and then solve the convection diffusion equation, Eq. (59), for the sample ions as a passive tracer. First, we look at the effect of diffusion in our single-channel model. In Fig. 12, we show maximum theoretical enhancement using the same parameters as Fig. 10, but we add two calculations corresponding to diffusion of the sample ions at a Peclet number selected to match applied electric fields of 16 kV/m (dotted) and 32 kV/m (dashed). With this plot, we can start to understand quantitatively why a higher electric field shows a higher enhancement in a nanochannel, but why there is no effect in a microchannel. The width of the concentrated sample is simply the initial length divided by the enhancement factor (with no focusing effect). Diffusion decreases the maximum enhancement because the local axial Peclet number (based on the concentrated sample width) becomes small. Using a simple argument, we can estimate the maximum enhancement in the regime of no sample focusing. First, we note that the time scale for the sample ions to leave the low-conductivity region is $t=L_{s,0}/(U_\sigma-U_{s,\mathrm{low}})$ where $L_{s,0}$ is the length of the sample region initially, $U_{s,\mathrm{low}}$ is the sample velocity in the low-conductivity region, and U_σ is the velocity of the conductivity interface. The length scale for diffusion of the sample ions is $\sqrt{Dt}$, where D is diffusivity of sample ions. Thus, the best enhancement you can expect to achieve is approximately $L_{s,0}/\sqrt{Dt}$ that would occur at the instant the low-conductivity region is cleared of sample ions. After this point, diffusion can only decrease the enhancement over time. These scaling arguments may provide guidance for future developments of nanofluidic FASS in order to achieve higher concentration enhancement.

When the sample is being focused, we can find a quasi-steady state solution for distribution of the sample ions assuming the background salt is stationary. At a quasi-steady state, the sample ions have no flux, i.e.,

$$\overline{un_s}+b_s\bar{n}E-\frac{1}{\mathrm{Pe}_L}\frac{\partial\bar{n}_s}{\partial x}=0, \tag{60}$$

which can be rewritten in the frame of reference moving with the interface,

$$U=\frac{1}{\mathrm{Pe}_L}\frac{\partial\ \ln(\bar{n}_s)}{\partial x}, \tag{61}$$

where the sample velocity is defined as $U=j_n/\bar{n}_s-U_\sigma$ and the Peclet number based on the channel length is $\mathrm{Pe}_L=U_0L/D$. If the interface between the high- and low-conductivity regions is taken to be sharp, then U can be considered to be constant on both sides of the interface, and the concentration of sample ions follows a simple Boltzmann drift-diffusion balance:

$$\bar{n}_s=\mathrm{e}^{Ux/\mathrm{Pe}_L}. \tag{62}$$

In this case, the maximum value of enhancement in the interface is found easily from integration on both sides of the interface

$$\bar{n}_s=\mathrm{Pe}_{L,1}/U_1+\mathrm{Pe}_{L,2}/U_2. \tag{63}$$

The result above is easily generalized if the conductivity interface is not sharp. If the conductivity interface is diffuse, then the "force" pushing the sample ions to the focus point is lessened and the concentration enhancement is decreased. This effect is shown in Fig. 13 where we show the quasi-steady sample ion distributions in the focused regime for different interface thicknesses. Even modest amounts of spreading of the background conductivity can significantly reduce the maximum sample concentration.

The evolution of the spatial shape of the electrical conductivity field is an interesting area for future study. Recent work by Mani and co-workers[38,39] showed that concentration shocks can originate from a micro/nanochannel junction and propagate through the system. Their analysis very generally predicts concentration shocks forming in a simple channel when moving from a region of high to low ionic strength (conductivity), a situation realized in FASS [see the schematic in their Fig. 5 (Ref. 38)]. Their predictions imply that the trailing edge of the low/high conductivity interface in FASS would sharpen due to shock formation, while the leading edge would spread. This behavior is also predicted by a simple extension of our model. Instead of assuming the conductivity of the two regions is simply a single jump from 10 to 1, we can assume the conductivity changes in smaller discrete steps (e.g., the conductivity goes from 10 to 5 to 1). We can then plot the propagation speed of all the jumps in conductivity just as was done in Fig. 9. This analysis shows the characteristics of the conductivity interfaces *converging* in the trailing edge and *diverging* at the leading edge. This sharpening of the trailing edge of the conductivity region is advantageous to FASS since the shock formation mechanism will maintain a sharp conductivity gradient at the trailing edge where it is needed most. The formation and propagation

Downloaded 11 Mar 2011 to 209.94.128.116. Redistribution subject to AIP license or copyright; see http://pof.aip.org/about/rights_and_permissions

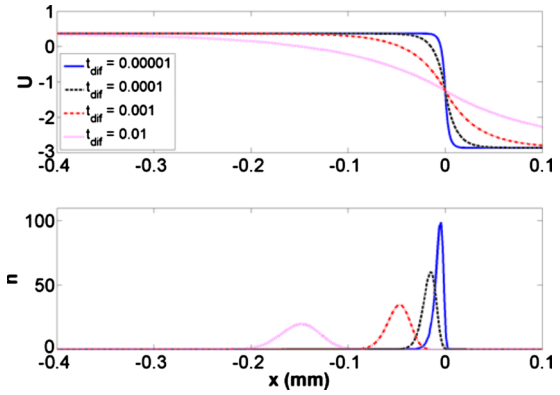

FIG. 13. (Color online) (top) Speed of sample ions relative to the interface speed as a function of position. The different curves are for diffusion times of 0.01, 0.001, 0.0001, and 0.000 01. For our system this corresponds to the conductivity interface existing for 10, 1, 0.1, and 0.01 s, respectively. If there is no diffusion of the interface then the maximum value of the sample concentration is 217 in this example. We see that even modest amounts of diffusion significantly reduce the sample concentration. (bottom) The quasisteady state distribution of sample ion concentration, n, as a function of position for the corresponding diffuse interfaces. The peak will always be located where the velocity in (top) passes through 0.

of shocks in the background fluid is yet another area for future study.

Finally, we can account for diffusion of the sample ions in our full 4 channel model to match our simulations with data. In Fig. 14, we show the simulation results accounting for diffusion that mimics the conditions for the experimental data. In this figure we compare results in the 250 nm and 1 μm deep channel at different electric fields. Recalling the experimental data in Fig. 5, the model shows the proper trends and shows reasonable quantitative agreement. The nanochannel shows clearly more enhancement of the sample on the same order of magnitude as the experiments. The time scales and shapes of the peak are also in general agreement. The exact results are quite sensitive to the parameters selected for the surface charge and the gating scheme, thus perfect agreement is difficult to obtain.

VII. CONCLUSIONS

In this paper, we have examined the effects of the electric double layer on sample preconcentration in nanofluidic channels. When the electric double layer is finite in size relative to channel height, the sample ions that possess the same charge as the wall are repelled, and thus their average flow velocity is different from the mean flow. Due to pressure gradients inherent in FASS systems, we predict the existence of a focusing effect at the conductivity interface, where sample ions in the low-conductivity region are slower than the mean velocity of the region, and sample ions in the high-conductivity region are faster than the mean velocity in that region. The existence of the focusing effect is supported by the experimental evidence. Even in regimes where focusing is not present, the nanochannel model and experiment demonstrate significantly better concentration enhancement relative to the microchannel. While the concentration enhancement in a nanochannel is higher, there are certainly many applications where microchannel FASS would be remain the preferred technique due to the challenges of inherently low signals that occur in nanofluidic systems.

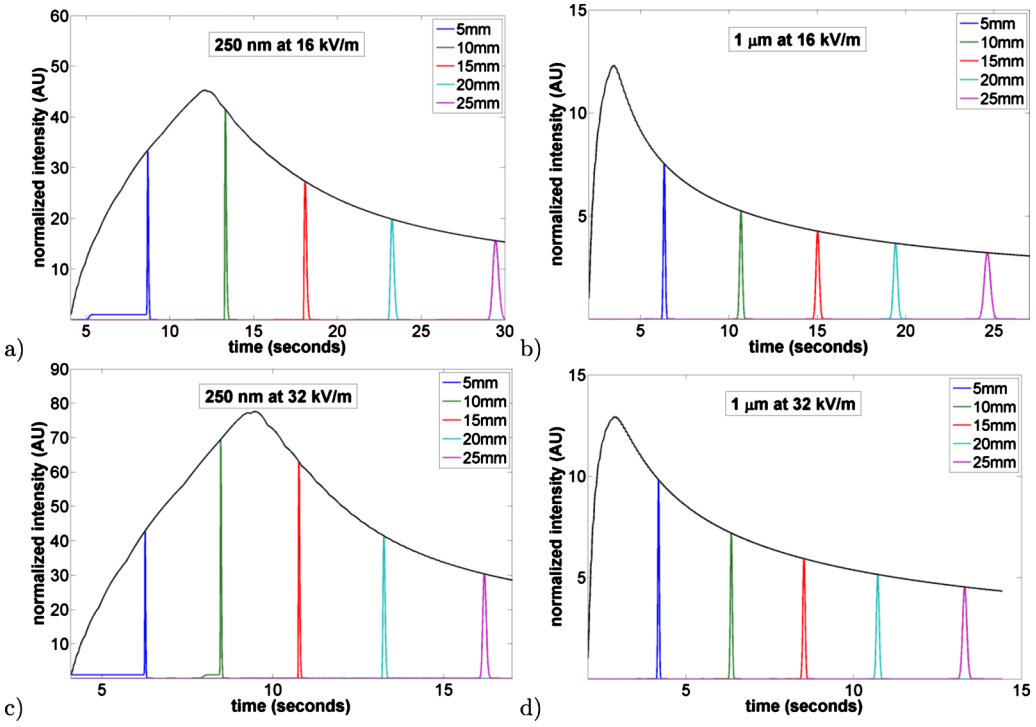

FIG. 14. (Color online) Data from the model with diffusion simulating the experimental conditions of Fig. 5. Here we show the time history of the concentration of sample at different locations of 5, 10, 15, and 20 mm downstream. The concentrations are 1 and 10 mM in all four figures. The top curve shows the maximum concentration in the channel at that instant of time. (a) 250 nm channel at 16 kV/m, (b) 1 μm channel at 16 kV/m, (c) 250 nm channel at 32 kV/m, and (d) 1 μm channel at 32 kV/m. These simulations replicate the main features of the experimental data.

Downloaded 11 Mar 2011 to 209.94.128.116. Redistribution subject to AIP license or copyright; see http://pof.aip.org/about/rights_and_permissions

Furthermore, we investigate the effects of gating a sample in a four-channel geometry in order to obtain quantitative agreement between our data and theory. We note that the theoretical model is quite sensitive to gating time and length of plug injected, which were parameters that were not very well controlled in the current experiments. However, even with current uncertainties, we have obtained good agreement with all the trends observe in experiments. Finally, we end this paper with some notes on adding diffusion to the model, which can both qualitatively and quantitatively match data and trends well, especially capturing the effect of electric field on concentration enhancement.

This work also points to future directions and challenges. Diffusion and dispersion should be added the model in a more formal way. The simple model presented here clearly has the ability to explain the basic phenomena of FASS in nanofluidic channels, however this work has also shown that to obtain quantitative agreement with the experiments properly capturing diffusive effects is critical. While it seems reasonable to ignore dispersion in the shallow direction of the channel, dispersion in the width direction may play an important role.[52] A clearer understanding of the dynamics of the steepening of the conductivity gradient and the formation of concentration shocks could yield better predictions of sample stacking and focusing and possibly lead to new insight that could be leveraged in application. Further it would be useful to obtain better predictions and a better understanding of the gating process. Currently, the amount of sample injected in the channels is uncontrolled, which makes fitting the experimental data challenging. These uncertainties make it difficult to assess the quantitative power of the current modeling framework. Modeling of the details of the gating process at the cross junction beyond our simple 1D model may be required to obtain better agreement between theory and experiment.

However, despite clear areas for advancement, our simple model predicts the key trends that are found in the experiments, namely, that nanochannel FASS generally outperforms microchannel FASS and that enhancement in nanochannels is improved both at lower background concentrations (thicker double layers) and higher electric fields. In microchannels where double layers are thin, the sample enhancement is only a function of the conductivity ratio. Nanochannels display a rich set of behavior that can potentially be leveraged for new applications.

ACKNOWLEDGMENTS

This work was supported by the start-up funds of SP. B.D.S. would like to thank the ME department at UC Santa Barbara for hosting him as a visitor while this work was initiated. The authors thank Martin Bazant for pointing out the connection between our work and that of Ref. 38.

[1]T. M. Squires and S. R. Quake, "Microfluidics: Fluid physics at the nanoliter scale," Rev. Mod. Phys. **77**, 977 (2005).
[2]G. M. Whitesides, "The origins and the future of microfluidics," Nature (London) **442**, 368 (2006).
[3]R. B. Schoch, J. Han, and P. Renaud, "Transport phenomena in nanofluidics," Rev. Mod. Phys. **80**, 839 (2008).
[4]A. van den Berg, H. G. Craighead, and P. Yang, "From microfluidic applications to nanofluidic phenomena," Chem. Soc. Rev. **39**, 899 (2010).
[5]M. Napoli, J. C. T. Eijkel, and S. Pennathur, "Nanofluidic technology for biomolecule applications: A critical review," Lab Chip **10**, 957 (2010).
[6]S. Pennathur and J. G. Santiago, "Electrokinetic transport in nanochannels 1: Theory," Anal. Chem. **77**, 6772 (2005).
[7]S. Pennathur and J. G. Santiago, "Electrokinetic transport in nanochannels 2: Experiments," Anal. Chem. **77**, 6782 (2005).
[8]R. F. Probstein, *Physicochemical Hydrodynamics: An Introduction* (Wiley, New York, 1994).
[9]S. Pennathur, F. Baldessari, J. G. Santiago, M. G. Kattah, J. B. Steinman, and P. J. Utz, "Free-solution oligonucleotide separation in nanoscale channels," Anal. Chem. **79**, 8316 (2007).
[10]J. D. Cross, E. A. Strychalski, and H. G. Craighead, "Size-dependent DNA mobility in nanochannels," J. Appl. Phys. **102**, 024701 (2007).
[11]J. Han and H. G. Craighead, "Separation of long DNA molecules in a microfabricated entropic trap array," Science **288**, 1026 (2000).
[12]E. A. Strychalski, H. W. Lau, and L. A. Archer, "Nonequilibrium separation of short DNA using nanoslit arrays," J. Appl. Phys. **106**, 024915 (2009).
[13]W. Reisner, N. B. Larsen, H. Flyvbjerg, J. O. Tegenfeldt, and A. Kristensen, "Directed self-organization of single DNA molecules in a nanoslit via embedded nanopit arrays," Proc. Natl. Acad. Sci. U.S.A. **106**, 79 (2009).
[14]S. M. Stavis, E. A. Strychalski, and M. Gaitan, "Nanofluidic structures with complex three-dimensional surfaces," Nanotechnology **20**, 165302 (2009).
[15]F. E. P. Mikkers, F. M. Everaerts, and Th. P. E. M. Verheggen, "High performance zone electrophoresis," J. Chromatogr. A **169**, 11 (1979).
[16]R. L. Chien and D. S. Burgi, "Sample stacking of an extremely large injection volume in high-performance capillary electrophoresis," Anal. Chem. **64**, 1046 (1992).
[17]R. L. Chien and D. S. Burgi, "On-column sample concentration using field amplification in CZE," Anal. Chem. **64**, 489A (1992).
[18]R. Bharadwaj and J. G. Santiago, "Dynamics of field-amplified sample stacking," J. Fluid Mech. **543**, 57 (2005).
[19]C. H. Lin and T. Kaneta, "On-line sample concentration techniques in capillary electrophoresis: Velocity gradient techniques and sample concentration techniques for biomolecules," Electrophoresis **25**, 4058 (2004).
[20]Y. Yang, R. I. Boysen, and M. T. W. Hearn, "Optimization of field-amplified sample injection for analysis of peptides by capillary electrophoresis-mass spectrometry," Anal. Chem. **78**, 4752 (2006).
[21]L. Zhang and X.-F. Yin, "Field amplified sample stacking coupled with chip-based capillary electrophoresis using negative pressure sample injection technique," J. Chromatogr. A **1137**, 243 (2006).
[22]J. L. Beckers and P. Bocek, "Sample stacking in capillary zone electrophoresis: Principles, advantages and limitations," Electrophoresis **21**, 2747 (2000).
[23]R. L. Chien, "Sample stacking revisited: A personal perspective," Electrophoresis **24**, 486 (2003).
[24]H. Yang and R. L. Chien, "Sample stacking in laboratory-on-a-chip devices," J. Chromatogr. A **924**, 155 (2001).
[25]C. L. Ren and D. Li, "Electrokinetic sample transport in a microchannel with spatial electrical conductivity gradients," J. Colloid Interface Sci. **294**, 482 (2006).
[26]S. Song and A. K. Singh, "On-chip sample preconcentration for integrated microfluidic analysis," Anal. Bioanal. Chem. **384**, 41 (2006).
[27]R. Bharadwaj, J. G. Santiago, and B. Mohammadi, "Design and optimization of on-chip capillary electrophoresis," Electrophoresis **23**, 2729 (2002).
[28]S. C. Jacobson and J. M. Ramsey, "Microchip electrophoresis with sample stacking," Electrophoresis **16**, 481 (1995).
[29]B. Jung, R. Bharadwaj, and J. G. Santiago, "Thousandfold signal increase using field-amplified sample stacking for on-chip electrophoresis," Electrophoresis **24**, 3476 (2003).
[30]H. Lin, B. D. Storey, M. H. Oddy, C. H. Chen, and J. G. Santiago, "Instability of electrokinetic microchannel flows with conductivity gradients," Phys. Fluids **16**, 1922 (2004).
[31]C.-H. Chen, H. Lin, S. K. Lele, and J. G. Santiago, "Convective and absolute electrokinetic instability with conductivity gradients," J. Fluid Mech. **524**, 263 (2005).
[32]H. Lin, B. D. Storey, and J. G. Santiago, "A depth-averaged model for electrokinetic flow in microchannels," J. Fluid Mech. **608**, 43 (2008).

Downloaded 11 Mar 2011 to 209.94.128.116. Redistribution subject to AIP license or copyright; see http://pof.aip.org/about/rights_and_permissions

[33]J. J. Santos and B. D. Storey, "Instability of electroosmotic channel flow with streamwise conductivity gradients," Phys. Rev. E **78**, 046316 (2008).
[34]C. F. Ivory, "A brief review of alternative electrofocusing techniques," Sep. Sci. Technol. **35**, 1777 (2000).
[35]P. G. Righetti and A. Bossi, "Isoelectric focusing of proteins and peptides in gel slabs and in capillaries," Anal. Chim. Acta **372**, 1 (1998).
[36]A. E. Herr, J. I. Molho, K. A. Drouvalakis, J. C. Mikkelsen, P. J. Utz, J. G. Santiago, and T. W. Kenny, "On-chip coupling of isoelectric focusing and free solution electrophoresis for multidimensional separations," Anal. Chem. **75**, 1180 (2003).
[37]D. Ross and L. E. Locascio, "Microfluidic temperature gradient focusing," Anal. Chem. **74**, 2556 (2002).
[38]A. Mani, T. A. Zangle, and J. G. Santiago, "On the propagation of concentration polarization from microchannel-nanochannel interfaces. Part I. Analytical model and characteristic analysis," Langmuir **25**, 3898 (2009).
[39]T. A. Zangle, A. Mani, and J. G. Santiago, "On the propagation of concentration polarization from microchannel-nanochannel interfaces. Part II. Numerical and experimental study," Langmuir **25**, 3909 (2009).
[40]Y.-C. Wang, A. Stevens, and J. Han, "Million-fold preconcentration of proteins and peptides by nanofluidic filter," Anal. Chem. **77**, 4293 (2005).
[41]C. T. Culbertson, S. C. Jacobson, and J. M. Ramsey, "Diffusion coefficient measurements in microfluidic devices," Talanta **56**, 365 (2002).
[42]A. Sze, "Zeta-potential measurement using the Smoluchowski equation and the slope of the current-time relationship in electroosmotic flow," J. Colloid Interface Sci. **261**, 402 (2003).
[43]T. Driehorst, P. O'Neill, D. Fygenson, and S. Pennathur, "Characterization of Agn: DNA nanoclusters by capillary electrophoresis in microfluidic channels," *Proceedings of the Thirteenth International Conference on Miniaturized Systems on Miniaturized Chemical and BioChemical Analysis Systems* (μTAS 2009), Jeju, Korea, 1–5 November 2009 (Chemical and Biological Microsystems Society, San Diego, California, 2009).
[44]M. Wang and A. Revil, "Electrochemical charge of silica surfaces at high ionic strength in narrow channels," J. Colloid Interface Sci. **343**, 381 (2010).
[45]M. Z. Bazant, M. S. Kilic, B. D. Storey, and A. Ajdari, "Towards an understanding of induced-charge electrokinetics at large applied voltages in concentrated solutions," Adv. Colloid Interface Sci. **152**, 48 (2009).
[46]V. G. Levich, *Physicochemical Hydrodynamics* (Prentice-Hall, Englewood Cliffs, NJ, 1962).
[47]J. N. Israelachvili, *Intermolecular and Surface Forces* (Academic, London, 1985).
[48]F. Baldessari and J. G. Santiago, "Electrokinetics in nanochannels. Part I. Electric double layer overlap and channel-to-well equilibrium," J. Colloid Interface Sci. **331**, 549 (2009).
[49]D. Burgreen and F. R. Nakache, "Electrokinetic flow in ultrafine capillary slits," J. Phys. Chem. **68**, 1084 (1964).
[50]C. L. Rice and R. Whitehead, "Electrokinetic flow in a narrow cylindrical capillary," J. Phys. Chem. **69**, 4017 (1965).
[51]R. Aris, "On the dispersion of a solute in a fluid flowing through a tube," Proc. R. Soc. Lond. A Math. Phys. Sci. **235**, 67 (1956).
[52]A. Ajdari, N. Bontoux, and H. A. Stone, "Hydrodynamic dispersion in shallow microchannels: The effect of cross-sectional shape," Anal. Chem. **78**, 387 (2006).

Downloaded 11 Mar 2011 to 209.94.128.116. Redistribution subject to AIP license or copyright; see http://pof.aip.org/about/rights_and_permissions